

Navigation Route Selection in Ice-Covered Waters

by

Marian Spiteri

A report

presented to the Canada Center for Inland Waters

Burlington, Ontario

Waterloo, Ontario, Canada, 1997

©Marian Spiteri 1997

Abstract

The recent increase in activity in the Canadian Arctic demands improvement in ice navigation technology. The ability to extend the shipping season safely into the winter season would be of great economic benefit to companies involved in mineral exploration and transportation.

Winter ice conditions in the Canadian Arctic create a dangerous environment for ship transit. The need arises for optimal routes through the ice which minimize the risk to the ship and the environment, and also minimizes schedule disruptions.

In this thesis, an automatic route selection system for navigation in ice-covered waters is developed and implemented. Features extracted from synthetic aperture radar imagery provide clues about the strength of the ice. The dynamic programming formulation encourages passage through weaker ice while simultaneously minimizing the distance of the voyage. The desirability of the suggested route is quantified by estimating the transit time of the vessel.

Acknowledgements

I am greatly indebted to Dr. B. Kerman of the Atmospheric Environment Service at the Center for Inland Waters for many helpful discussions. I would also like to express my sincere gratitude to my thesis supervisor Dr. M. E. Jernigan of the Department of Systems Design Engineering at the University of Waterloo for his helpful advice and guidance. I thank the faculty members and fellow graduate students of the Vision and Image Processing group who have aided my research with suggestions and advice. Funding for this work was provided by the Center for Inland Waters.

Contents

1	Introduction	1
1.1	Background	1
1.2	Operational Requirements	2
1.3	Information Sources	2
1.4	Specific Objectives of Report	3
1.5	Layout of Report	3
2	Properties of Sea Ice	5
2.1	Physical Properties of Sea Ice	6
2.2	SAR Signatures of Sea Ice	7
3	Data	11
3.1	Typical Ice Conditions in the Beaufort Sea in Winter	14
3.2	Visual Description of Ice Types in Image	15
4	Image Feature Extraction	17
4.1	Tonal Properties	18

4.2	Textural Properties	19
4.2.1	First-Order Textural Properties	20
4.2.2	Second-Order Textural Properties	23
4.3	Other Features	26
4.4	Comparisons	29
4.5	Summary	29
5	The Shortest Path Problem	31
5.1	Network Definition	31
5.2	Exhaustive Enumeration	32
5.3	Dijkstra's Method	32
5.3.1	Example of Dijkstra's Algorithm	33
5.3.2	Proof of Dijkstra's Method	37
5.3.3	Computational Efficiency of Dijkstra's Method	38
5.4	Modifications to Dijkstra's Procedure	39
5.4.1	Benefits of Modifications	40
5.4.2	Example of Modified Algorithm	40
5.5	Summary	44
6	Cost Assignment	46
6.1	Methodology	47
6.1.1	Selection of Features	47

6.1.2	Selection of Routes	56
6.1.3	Selection of Cost Functions	56
6.2	Results	61
6.3	Cost Assignment using Kerman's Exponential Relationship	66
6.3.1	Results	68
6.4	Conclusions	71
7	Vessel Performance	72
7.1	Ice Resistance	73
7.2	Velocity	74
7.3	Implementation and Results	75
7.3.1	Ice Parameters	75
7.3.2	Ship Parameters	76
7.3.3	The Routes	76
7.3.4	Conclusions	77
7.4	Future Work	80
8	Summary	85
A	Description of Some Sea Ice Features	87
A.1	First-Order Tonal Features	87
A.2	First-Order Texture Features	88
A.3	Second-Order Texture Features	89

B Glossary of Terms

91

Bibliography

95

List of Figures

3.1	Image #125 - L-band, HV polarization SAR - Beaufort sea	12
3.2	Image #125 - C-band, HH polarization SAR - Beaufort sea	13
4.1	Image sample used to calculate the GLD matrix	21
4.2	Image sample used to calculate the NGLD matrix	22
4.3	Image sample used to calculate the NGTDM	23
4.4	Image sample used to calculate the GLCM	24
4.5	Grey-level co-occurrence matrix for Figure 4.4	24
4.6	Image sample used to calculate the Kerman probability matrix. . .	27
5.1	Network Example	34
6.1	Intensity histograms for 3 ice types.	49
6.2	Standard Deviation histograms for 3 ice types.	49
6.3	Weszka's Entropy feature histograms for 3 ice types.	50
6.4	Weszka's Mean feature histograms for 3 ice types.	50
6.5	Haralick's Contrast feature histograms for 3 ice types.	51

6.6	Haralick's Entropy feature histograms for 3 ice types.	51
6.7	Standard Deviation image of SAR image.	53
6.8	Weszka's Entropy feature.	53
6.9	Weszka's Mean feature.	54
6.10	Haralick's Entropy feature.	54
6.11	Haralick's Contrast feature.	55
6.12	End-points of the three paths.	57
6.13	Probability of ice type, tonal feature.	60
6.14	Path 1 using tone feature and threshold cost function.	62
6.15	Path 2 using tone feature and threshold cost function.	62
6.16	Path 3 using tone feature and threshold cost function.	63
6.17	Path 3 using Tone feature and Linear cost function.	65
6.18	Path 3 using Haralick's Contrast feature and Quartic cost function.	65
6.19	Joint probability distribution, $P(51, j)$	67
6.20	Logarithm of $P(51, j)$ and the exponential overlay P_{est}	67
6.21	Path 1 using Kerman's bonding probability.	69
6.22	Path 2 using Kerman's bonding probability.	70
6.23	Path 3 using Kerman's bonding probability.	70
7.1	Segmentation of image chh125 into 3 ice types.	76
7.2	Path 1 using the transit time, M.V. Arctic.	78
7.3	Path 2 using the transit time, M.V. Arctic.	78

7.4	Path 3 using the transit time, M.V. Arctic.	79
7.5	Path 1 using the transit time, L.S.S. Laurent.	79

List of Tables

3.1	Statistics of the Beaufort Sea	14
6.1	End-Points	56
6.2	Thresholds	58
6.3	Summary of Results	64
7.1	Ice Thickness	76
7.2	Ice Data	77
7.3	Ship Parameters	80
7.4	Results	81
7.5	Notation	84

Chapter 1

Introduction

1.1 Background

Remote sensing of ice-covered regions is the subject of extensive research in Canada. Beneficiaries of sea ice information include industries involved in the exploration and transportation of petroleum and mineral resources in the Canadian Arctic, commercial shipping companies, scientists studying the importance of ice in the environment, the fisheries, and the Canadian Coast Guard.

Vessels negotiating high ice-concentration waters risk colliding with ice or being beset in ice. Possible accompanying costs are excessive consumption of fuel, economic loss due to serious delays, damage to the vessel, environmental disaster, and loss of life. Ice can be avoided with better knowledge of its location and strength.

1.2 Operational Requirements

The operational requirements of vessels traversing ice-covered waters are divided into strategic, tactical, and close-range hazard detection information [1].

Strategic information is used for long-range planning of vessel routing. In the months prior to the voyage, shore-based analysis of historical trends is undertaken to assess ice conditions along the intended route. Included in the analysis is the ship's expected performance under the anticipated ice conditions. Weeks before the voyage, information is collected on the existing ice conditions along the shipping channels and the existing meteorological conditions. Using historical evidence, existing ice conditions, and meteorological data, the conditions at the time of the voyage are forecast. As the commencement of the voyage draws near, the forecast of the ice conditions is compared to the actual developing conditions and updated as necessary.

Tactical information is gathered about portions of the route that contain difficult ice one or two days ahead of the ship in transit. The information includes the type, concentration and ridging of the ice up ahead. This information is used to select a good route through or around the difficult ice.

Close-range ice hazard detection information alerts the helm about ice conditions in the immediate vicinity of the vessel. This information enables the ship to avoid impact with small but dangerous ice hazards in its path.

1.3 Information Sources

In the past, the ship's navigator was informed of the ice around the ship by lookouts in the crow's nest. Today, a sophisticated arrangement of data sources obtained

during each of the strategic, tactical and close-range elements of an ice navigation strategy is used to provide more accurate information.

At the strategic planning level, information is obtained from historical sources, satellite imagery, long-range patrol aircraft, and ice charts. At the tactical level, information can be provided by other ships upstream, or from an aircraft flying over the route. At the close-range detection level, on-board marine radar is predominantly used to monitor the immediate ice conditions.

1.4 Specific Objectives of Report

The objective of this report is the construction and analysis of an automatic routing program for vessel transit in ice-covered waters. The transit routes are generated using information found in remotely-sensed Synthetic Aperture Radar (SAR) images and specific knowledge of the area and vessel. The specific knowledge is gathered from historical data on ice conditions in the region and the expected performance of the vessel in those ice conditions. Reducing the reliance on manual photo interpretation will allow real-time processing of information and consistent output that does not depend on the human interpreter. An automatic route generator would be of use during the strategic and tactical information collection stages.

1.5 Layout of Report

Chapter 2 presents an introduction to the physical properties of the three major sea ice types: young ice, first-year ice and multi-year ice. In addition, the interactions between the ice and the microwaves transmitted by the SAR imaging system are

discussed. The SAR image data used in this report is displayed and interpreted in Chapter 3. The ice conditions typically found in the Beaufort Sea during the winter season are also presented. Chapter 4 investigates several methods that are commonly used to generate features needed to classify the ice in the image. The type of ice provides some knowledge of the properties of the ice such as thickness and strength which are important parameters for the selection of an optimal route. Chapter 5 interprets the SAR image as a network and describes Dijkstra's method for finding the optimal path joining two nodes in a network. In Chapter 6, the network links are assigned costs that reflect the ice conditions using the features of Chapter 4. Then, Dijkstra's method is invoked to generate optimal routes between two pixels in the image. In Chapter 7, each link in the SAR image network is assigned a value corresponding to the traversal time of a real vessel. Optimal routes are generated by minimizing the traversal time. Chapter 8 concludes the report with a summary and recommendations for future work.

Chapter 2

Properties of Sea Ice

This chapter introduces the properties of sea ice that affect the synthetic radar (SAR) returns captured on a SAR sea ice image. Differences in properties such as salinity, density, snow cover, topography, and thickness of ice can be sensed by SAR, but the extraction of quantitative values of ice properties is not possible. A SAR sensor measures the backscatter, which in the case of sea ice is largely due to surface and volume scattering. The degree of surface scattering depends on surface roughness and variations in the dielectric properties of the ice caused by salinity levels. Volume scattering occurs in the presence of discontinuities such as gas bubbles in the ice medium.

Sea ice can be classified into three distinct categories: open water/young ice, first-year ice, and multi-year ice. Young and first-year ice occur in the current year and multi-year ice has survived a summer melt season. Each ice category is known to have distinctly different microwave backscatter returns that can form the basis of classification.

2.1 Physical Properties of Sea Ice

Sea ice crystals form at temperatures close to -2°C . The crystals float to the surface of the water where they coalesce and form a solid surface layer up to 30 cm thick called young ice [2]. Salt is expelled during the freezing process so that the crystals are of pure ice. However brine becomes trapped in elongated vertical brine pockets within the solid ice matrix. As the ice ages, the brine tends to migrate downwards under the influence of gravity. Thus, with age, sea ice becomes progressively less saline and stronger as the brine pockets disappear.

Ice undergoes extensive mechanical deformation from impact with other ice due to forces of wind, waves, and ocean currents. Colliding ice sheets that are less than one meter in thickness [3] will form ice rafts where one ice sheet slides on top of the other. Thicker ice sheets usually buckle under the force of impact. The buckling may occur at the point of contact of the two ice sheets or along a line where the ice is mechanically weak. Ice is very brittle and fracture results in ridges of angular blocks. Ridges in first-year ice reach heights in the range of two meters [3]. Ridges tend to be long linear features whose lengths may be in the kilometer range but whose widths are typically only in the tens of meters. Rubble occurs when ridged ice sheets undergo the forces of compression and shear so that repeated ridging events occur. Estimates from submarine surveys indicate that 25% to 50% of all Arctic ice is contained in ridges [4].

At the start of the summer melt season, snow on the surface of the ice begins to melt. When all the snow has melted, between 75% and 95% of the surface of the first-year ice will be covered with several centimeters of fresh water [3]. As the temperature continues to increase, the sea ice starts to melt. Some ice floes will melt completely, but some will survive the summer melt season. At the start of the

new growth season, the salinity of the surviving ice has been significantly reduced due to flushing from fresh surface water. This ice is clear and very hard and is known as multi-year ice.

Multi-year ice has a characteristic undulating appearance. The higher ice features are called hummocks and the lower features are re-frozen melt ponds. Pressure ridges formed in the current season are also present. Hummocks are smooth, raised features on the ice surface. They are the remains of deformed first-year ice such as rubble, ridges and rafted ice. The angular blocks of broken first-year ice become weathered during the melting period and the ice blocks are consolidated. The resulting hummocks are very strong. Hummocks have low salinities because their height allows gravity to drain the brine cavities during the summer. Melt ponds are formed primarily from melted surface snow and can be up to 20 centimeters deep [3]. The melt water absorbs more radiation than the surrounding ice and gradually deepens as the surface ice under the pond begins to melt. Much of the water from melt ponds will drain into cracks or holes in the ice, but some remains to refreeze in the winter. Melt water is fresh water and the resulting ice has zero salinity. The average thickness of undeformed multi-year ice is 3 to 4 m [5], but deformed multi-year ice thickness varies greatly. A multi-year ice floe can have thicknesses ranging from less than a meter to tens of meters [6].

2.2 SAR Signatures of Sea Ice

Synthetic aperture radar sensors are used to image sea ice in the Arctic. SAR sensors operate in the microwave portion of the electromagnetic spectrum at wavelengths from 2 to 24 cm [7]. These wavelengths are unaffected by adverse atmospheric conditions found in the arctic regions such as cloud cover, fog, and dark-

ness [8].

In order to interpret remotely sensed observations of sea ice, it is necessary to understand the relationships between the variations in the microwave signatures and the physical properties of the various ice types. The different ice types develop distinct surface features and exhibit properties such as salinity, density, and topography. If these ice properties could be sensed, then they would be useful as features in the classification. Experimentation and operational use has shown that SAR backscatter is sensitive to the physical properties of sea ice but the complete mapping between microwave signatures and ice properties has not been discovered. However, some correlations between ice properties and microwave signatures are known and will be discussed in this section.

Thin young ice is very saline and conforms to the shape of the water surface. In the open ocean, the water surface is affected by wind, currents, and waves and can be very rough. However, water that is shielded from the wind by surrounding ice floes has a smooth surface with correspondingly weak backscatter returns. As a result, open water and young ice within an ice pack have a dark representation in the image.

First-year sea ice has a salinity of between 5 and 20 ppm [3]. The high salinity makes first-year ice a high-loss dielectric medium that strongly attenuates microwave energy. There is little penetration of the microwaves into the first-year ice so any signal returns will be the result of surface scattering [3]. First-year ice can be smooth or heavily deformed. With smooth first-year ice, very little energy can be expected to return to the sensor. Thus, smooth first-year ice appears dark in a SAR image. Rough first-year ice presents a highly reflective surface and high returns are expected. Pressure ridges in rough first-year ice act as strong radar reflectors that appear as bright lines in a SAR image.

The weathered hummocks on the surface of multi-year ice do not reflect radar as strongly as first-year ice ridges. However, the lower salinity of multi-year ice (between 0 and 3 ppm [3]) allows radar waves to penetrate deeply into the ice. This penetration will allow the radar wave to interact with the inhomogeneities in the ice. The upper layers of multi-year ice contain air bubbles approximately 1-2 mm in diameter that act as internal discontinuities and cause significant radar backscatter [7]. The backscatter will increase as the number and diameter of the gas bubbles increases.

Multi-year melt pools have very smooth surfaces with density and salinity close to that of pure ice. The backscatter of melt pools is very weak because of the small surface and volume scattering. The intensity of the backscatter return from hummocks and melt pools differs by a factor of about 32 [7]. As a result, multi-year ice appears rough in texture in a SAR image.

An important consideration is the effect of the snow cover on backscatter returns. Snow cover can mask underlying ice features so that surface roughness is hidden to the sensor [7]. A heavy burden of snow can submerge and flood an ice floe with seawater, thereby altering the surface properties of the ice. The fresh meltwater from snow also changes the backscatter response. Thus, the presence of snow affects the backscatter response and subsequently hinders the process of ice type discrimination.

In summary, the dominant backscatter processes of each of the three main ice types are substantially different. When attempting to discriminate between the three ice types, the following information can be exploited:

- Multi-year ice backscatter returns are dominated by volume scatter because of the low density in the upper portion of multi-year ice sheets caused by the presence of gas bubbles.

- First-year ice produces strong surface scatter due to the surface roughness. Any increases in the scale of surface roughness will produce large changes in backscatter returns.
- Young ice and open water produce weak backscatter returns because of the smooth surfaces.

Chapter 3

Data

The synthetic aperture radar imagery used in this report was obtained with the NASA/JPL multifrequency, multipolarization airborne SAR system [9] on March 11, 1988 during the maximum ice extent. The two images depicted in Figures 3.1 and 3.2 representing the same scene but in two different frequencies and polarizations. Figure 3.1 is an L-band (1.28 GHz) Horizontal-Vertical (HV) polarization image and Figure 3.2 is a C-band (5.3 GHz) Horizontal-Horizontal (HH) polarization image. The site is located in the Beaufort sea at approximately 76° north latitude and 140° west longitude [10]. The images contain 400 pixels in the azimuth direction (left to right), and 400 pixels in the range direction (top to bottom). Each pixel covers an area of approximately 12.5 m by 12.5 m [11].

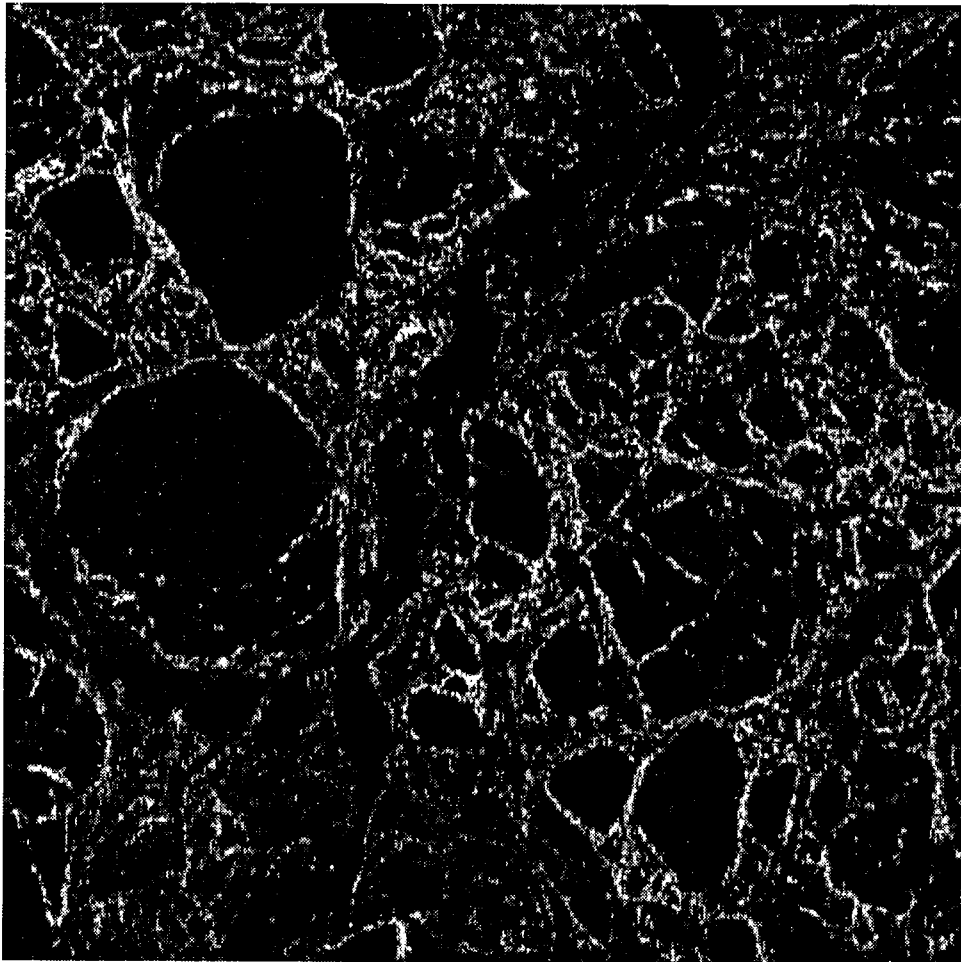


Figure 3.1: Image #125 - L-band, HV polarization SAR - Beaufort sea

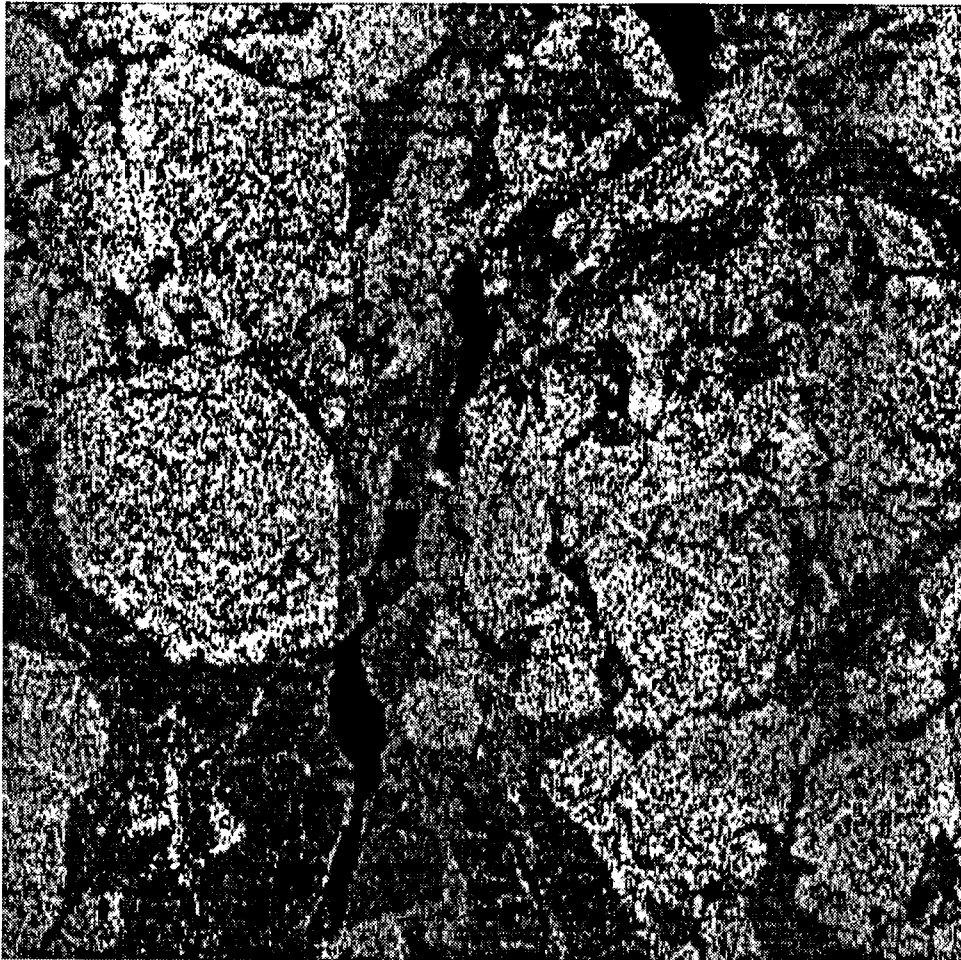


Figure 3.2: Image #125 - C-band, HH polarization SAR - Beaufort sea

3.1 Typical Ice Conditions in the Beaufort Sea in Winter

The Beaufort sea contains first-year and multi-year pack ice [3]. Much of the Beaufort Sea exploration occurs in the dynamic region known as the transition zone [3]. In the transition zone, the ice moves very quickly with mean ice velocities of 3.0 to 13.0 km per day [12], and suffers heavy ridging and deformation. Multi-year ice significantly impedes navigation by even ice-breaking vessels, and is a real threat to the structural integrity of vessels [3]. Nearshore multi-year ice floes are about 1 km in diameter. Further offshore, floe diameters in the range of 10-20 km have been reported [13]. In the winter, water might only be present in open leads for a few hours before it freezes [14].

The following sea ice data (Table 3.1) was compiled by Bercha [15] and gives a good indication of ice floe dimensions in the Beaufort sea.

Table 3.1: Statistics of the Beaufort Sea

Ice Type		Ridge Sail Height, m	Ice Floe Thickness, m	Ice Floe Size, m^2
First-year	mean	4.1	1.8	5×10^4
	maximum	9.9	2.9	3.7×10^7
Multi-year	mean	3.3	2.2	1.0×10^3
	maximum	8.9	5.2	1.2×10^6

3.2 Visual Description of Ice Types in Image

Since *in situ* verification of this report's work is impossible, interpretation of the images is based only on visual inspection. Many researchers have used the 1988 NASA/JPL data set [9, 10, 11, 16, 17]. This collection of papers provides a detailed description of the features in the data set.

Three ice types are present in the image: multi-year ice, first-year ice, and frozen lead ice. First-year ice can be further divided into rough and smooth ice. The rounded features visible in both images are multi-year ice floes. In the C-band imagery (Figure 3.2) the multi-year floes are very bright because of the high backscatter penetration of the radar into the upper layer of the ice where volume scattering occurs from millimeter-sized gas bubbles present within the ice. Both images represent the high, weathered ridges and adjacent melt ponds of multi-year ice with mottled tones of grey. In Figure 3.1, the multi-year ice floes are rimmed by brighter ice which is likely deformed first-year ice segments that are frozen to the large floes. In Figure 3.2, both multi-year and sheared first-year floe boundaries are characterized by bright tones. As a result, fragmented floe parts and rubble can be mistaken for multi-year ice floe fragments. In both images, smooth first-year ice appears darker than multi-year and first-year rubble. Structure from ridges and cracks in the first-year ice is very evident in the bright, linear features of the L-band image 3.1. The darkest regions in Figure 3.2 are smooth, young ice (leads) that are created by divergence in the ice pack [7]. Ambiguity occurs in the L-band image (Figure 3.1) between smooth first-year ice and lead ice but the C-band image shows high tonal discrimination between these two ice types.

To summarize, multi-year ice floes are very bright in the C-band image. The leads are very dark. Smooth and slightly deformed first-year ice is represented by a

medium grey tone. There is ambiguity between multi-year ice and broken first-year ice.

In the L-band image, first-year smooth ice can be mistaken for lead ice. Multi-year ice and rough first-year ice cannot be clearly differentiated by visual analysis. Ridges are very clearly delineated.

It is generally agreed that C-band imagery provides the best discrimination between first-year ice and multi-year ice [18]. For instance, the new Canadian satellite, RADARSAT, has been designed primarily for ice monitoring purposes and operates in C-band [18]. In navigation, it is most important to avoid multi-year ice floes at all costs. The C-band image in Figure 3.2 shows the dangerous multi-year ice floes clearly with a bright tone and high texture. Another item of importance is the location of leads that can be exploited by the ship. Leads are very clearly visible in C-band imagery because they are very dark and have little texture. The first-year ice has a medium grey tone, except for first-year rubble areas. These rubble areas can be mistaken for multi-year ice because they are so bright and the texture is similar to that of multi-year ice. However, such a mistake is an error on the cautious side and will not cause serious problems.

Chapter 4

Image Feature Extraction

Much research has been directed towards the development of sea ice classification algorithms [19, 20, 21, 22, 23, 24, 25, 26, 27, 28, 29]. Classification requires the extraction of a distinguishing characteristic or feature that clearly separates distinct ice types in the image. Such features are the result of specific manipulations or measurements of an image such as the intensity histogram, grey-level co-occurrence texture features, and spatial frequency spectra.

Two popular image properties used to describe image information are tonal and textural properties. The tonal properties represent the backscatter returns from the ice to the sensor. The textural properties describe the tonal variations within a small subsection of the image.

This chapter discusses several image features that have been used by researchers to separate ice types in SAR sea ice images. A small number of image features found in the literature that were used for purposes other than sea ice discrimination are also presented.

4.1 Tonal Properties

The first-order histogram of image intensity is the most basic feature that can be calculated from an image. The histogram equation is $A(b) = \frac{N(b)}{M}$, where M is the total number of pixels in a window and $N(b)$ is the number of pixels of intensity b in the window. The window may be the entire image or it may be a small region surrounding a pixel. Usually, the histogram of an entire SAR sea ice image will be unimodal even though several ice types are present [19], and thus, meaningful threshold values to segment the image are difficult to compute from the histogram. However, a small local histogram taken from a window surrounding a pixel will show a bimodal distribution if the window lies on the boundary of two ice types. From the bimodal histogram, the local area can be separated into distinct classes. The size of the window is very important because if the window is too large, more than two ice types may be represented and if it is too small, there will not be enough data to construct a good histogram. Sea ice classification techniques using local histograms are utilized in Wackerman *et al.* [19] and Haverkamp *et al.* [20].

In addition, various first-order tonal statistics can be used to describe histograms. Six statistics are suggested by Pratt [30]: mean, standard deviation, skewness, kurtosis, energy, and entropy. The definitions and formulae are listed in Appendix B. Barber [21], Lyden *et al.* [29], Nystuen and Garcia [24], and Shuchman *et al.* [25] explored the utility of tonal statistics in discriminating between sea ice types in SAR imagery. The statistics were computed for each ice type and then used to classify each pixel in the image. The results were mixed. Barber reported poor results, the findings of Lyden *et al.* were inconclusive, but Shuchman *et al.* and Nystuen and Garcia found that standard statistics do a good job of ice classification.

The most significant problem with classification based solely on grey tone from a single-band radar is the overlap of intensity groupings of different ice types. Studies have shown that the combination of textural information with tonal information improves image classification results for SAR sea ice [21], [26], [27].

4.2 Textural Properties

Although it is quite easy for humans to recognize and describe texture, it is very difficult to define texture in a concise mathematical way. The following collection of definitions demonstrates that texture is defined according to the particular application in which it is used.

- “The notion of texture appears to depend upon three ingredients: (i) some local ‘order’ is repeated over a region which is large in comparison to the order’s size, (ii) the order consists in the nonrandom arrangement of elementary parts, and (iii) the parts are roughly uniform entities having approximately the same dimensions everywhere within the textured region.” [31]
- “We may regard texture as what constitutes a macroscopic region. Its structure is simply attributed to the repetitive patterns in which elements or primitives are arranged according to a placement rule.” [32]
- “Texture could be defined as a structure composed of a large number of more or less ordered similar elements or patterns without one of these drawing special attention. So a global unitary impression is offered to the observer.” [33]

Haralick [34] emphasizes the interaction between tone (i.e. grey level) and texture in an image. He points out that tone and texture are simultaneously present

in the image, but depending on the circumstances, one or the other may dominate. When there is a large tonal variation in a small region of the image, texture becomes the dominant property. Where the region shows little tonal variation, the texture property is suppressed and the tone property dominates. Therefore, image texture is characterized by the tonal elements in combination with the spatial relationships between them.

The literature presents two main approaches to characterize texture: first-order and second-order texture measures. First-order measures are statistics such as variance and higher order moments that are calculated from information about the pixel's neighbourhood. First-order measures can also be obtained from one-dimensional vectors describing the tonal relationship between pixels in a small neighbourhood. Second-order texture measures are statistics that use two-dimensional matrices derived from the grey tone values of a window of pixels to describe the relationship between pixels.

4.2.1 First-Order Textural Properties

A simple first-order texture measure is the *standard deviation*. A small window is passed over the data and at each location, the standard deviation of the intensities inside the window is calculated and assigned to the central pixel. The size of the window is a significant consideration because if the window is too small, the statistics gathered will have little significance, while if the window is too large, multiple textural regions could be included.

Weszka *et al.* [35] describe four first-order measures used for terrain classification based on *Grey Level Difference (GLD)* statistics. The texture features are calculated from absolute differences between pairs of grey levels. Weszka *et al.*

```

3 2 1 2 0
2 3 0 1 2
3 2 1 0 2
1 2 1 1 2
3 2 3 1 1

```

Figure 4.1: Image sample used to calculate the GLD matrix

report that the gray level difference statistics perform as well as the more computationally expensive and complicated co-occurrence matrices (subsection 4.2.2) for their terrain classification application.

A small window is passed over the image and the probability distribution of intensity difference, $P(\delta_i)$, of pairs of pixels separated by distance, d , and angle, α , is estimated. Therefore each pixel in the image will be associated with a $P(\delta_i)$ such that the δ_i th component is the probability of finding an intensity difference of δ_i in the neighbourhood of the pixel.

In the example of Figure 4.1, if $d = 1$, $\alpha = 90^\circ$, and the window is 5×5 , then the GLD probability vector associated with the central pixel is:

$$P(0) = 2/20 = 0.1$$

$$P(1) = 14/20 = 0.7$$

$$P(2) = 3/20 = 0.15$$

$$P(3) = 1/20 = 0.05$$

If the texture is coarse and distance, d , is small, then the probability values near $\delta_i = 0$ will be high. A fine texture with a small distance, d , will display more spread in the probability distribution. Measures of texture may be found from measures of spread of the probability values around the origin. Weszka's four texture measures are listed and described in Appendix A.

$$\begin{array}{ccc} 3 & 2 & 1 \\ 2 & 3 & 0 \\ 3 & 2 & 1 \end{array}$$

Figure 4.2: Image sample used to calculate the NGLD matrix

Other features such as the variance, skewness and kurtosis, are also commonly extracted from the first-order GLD distribution [36].

The *Neighbouring Grey Level Dependence Matrix (NGLDM)* [37] is closely related to the GLD method but avoids the angular dependence. The NGLDM considers the relationship between the grey value of a pixel and its neighbouring pixels in all directions simultaneously. For example, in a 3×3 window, the intensity differences are calculated between each pixel in the window and the center pixel. Various texture features obtained from the NGLDM are presented in [23].

In the example of Figure 4.2, for a 3×3 window, the NGLDM probability vector is:

$$P(0) = 2/8 = 0.25$$

$$P(1) = 3/8 = 0.375$$

$$P(2) = 2/8 = 0.25$$

$$P(3) = 1/8 = 0.125$$

Amadasun and King [38] present the *Neighbourhood Grey-Tone Difference Matrix (NGTDM)* which is another relation of the GLD. In this case, for each intensity i found within a moving window, the difference is calculated between i and the average tone of the neighbours and summed over all instances of i . Amadasun and King present five texture features that are extracted from the NGTDM. They are coarseness, contrast, busyness, complexity, and texture strength.

3	2	1	2	0
2	3	0	1	2
3	2	1	0	2
1	2	1	1	2
3	2	3	1	1

Figure 4.3: Image sample used to calculate the NGTDM

In the example of Figure 4.3, the NGTDM vector is:

$$s(0) = \left|0 - \frac{12}{8}\right| + \left|0 - \frac{10}{8}\right| = 2.75$$

$$s(1) = \left|1 - \frac{8}{8}\right| + \left|1 - \frac{10}{8}\right| + \left|1 - \frac{11}{8}\right| + \left|1 - \frac{12}{8}\right| = 1.125$$

$$s(2) = 0.375$$

$$s(3) = 1.25$$

4.2.2 Second-Order Textural Properties

An often utilized second order statistic is the *Grey Level Co-occurrence Matrix* (GLCM) introduced by Haralick [39]. It has been used for automated SAR sea ice classification by a number of researchers including Holmes [26], Barber and LeDrew [22], Shokr [40], and Nystuen and Garcia [24].

A GLCM is computed from a small window for each pixel in the image. The GLCM contains the frequencies with which a pair of grey levels, separated by a distance, δ , and at an angle, θ , occur within the window. From the GLCM, various textural features can be extracted such as those proposed in [39], and [30]. Some commonly used second-order textural features for sea ice are given in Appendix A.

A small image sample in Figure 4.4 is used to illustrate the calculation of the grey-level co-occurrence matrix in Figure 4.5. The angle, θ , is 90° and the separation

3 1 2
2 1 0
3 2 0

Figure 4.4: Image sample used to calculate the GLCM

	0	1	2	3
0	0	0	0	0
1	1	1	0	1
2	1	1	0	0
3	0	1	1	0

Figure 4.5: Grey-level co-occurrence matrix for Figure 4.4

is 1.

Four parameters have to be selected in the GLCM approach: the size of the window, the direction (θ), the separation (δ), and the number of grey levels used in the GLCM. The size of the GLCM is given by the square of the number of grey levels. Using the full resolution may produce a GLCM that is very large, making the computations too expensive. However, if the number of grey levels is too small, the texture composition of the image sample will be harmed and the texture feature measures will not be effective. When a convolution window is to be used, the size of the window is always a difficult issue. Generally, if a texture is varying slowly, a large analysis window should be used. With a high-frequency texture, a smaller window should be used. No method has been established for selecting the distance or direction parameters. The optimal separation, δ , is found by comparing co-occurrence matrices for every δ ; however, this is not feasible. Generally, δ should be small for quickly varying textures and larger for slowly varying textures. The preferred orientation is data dependent and should reflect the angle containing the most useful information.

An early study by Holmes *et al.* [26] examined two GLCM texture features for

sea ice SAR images: inertia and entropy. The study found that first-year ice and multi-year ice could be differentiated with the inertial texture feature, while the entropy texture feature was able to characterize ice floe boundaries and regions of rough surface.

Shokr [40] and Barber and LeDrew [22] also applied Grey Level Co-occurrence Matrix texture measures to interpret SAR sea ice images. The research was aimed at determining the optimal combination of GLCM parameters and the best texture features for sea ice classification, where optimal is that which achieves maximum class separation.

Shokr computed the GLCM for various window sizes and interpixel distances. GLCMs were found for all four orientations (0° , 45° , 90° , and 135°) and then averaged. Shokr found that the GLCM texture features were insensitive to the size of the convolution window and to the interpixel distance. Using a fixed window size of 25×25 pixels, Barber and LeDrew found that a distance equal to one and an orientation angle in the look direction of the sensor provided the best results. Both groups quantized their images to four bits in order to reduce the computation time.

The features chosen by Shokr were grey tone, contrast, entropy, homogeneity, inverse difference moment, and maximum probability. Shokr conducted a univariate analysis to evaluate each individual texture statistic and found that the five GLCM texture features were highly inter-correlated, but they did not correlate with grey tone. Results showed that overall, the classification accuracy improved when grey tone and a texture feature were combined in a two-dimensional classification space. The inverse difference moment and entropy were found to provide the best classification accuracies.

Barber and LeDrew tested the discriminability of uniformity, correlation, entropy, dissimilarity, and contrast. In addition to a univariate analysis, they also conducted a multivariate analysis to determine if several texture statistics together would provide good discrimination of sea ice types. Results showed that the best discrimination occurred for a combination of any three texture features.

Nystuen and Garcia [24] compared SAR sea ice classification results using standard statistics (mean, range, standard deviation, skewness, kurtosis, and coefficient of variation of the pixel grey tones) and GLCM texture features (energy, correlation, inertia, cluster prominence, local homogeneity, and entropy). The research found that the standard statistics classified ice types with a higher accuracy than GLCM texture statistics. When the standard statistics features were used together with the GLCM features, accuracy improved marginally. However Nystuen and Garcia maintain that the improvement does not warrant the use of the computationally expensive GLCM texture features and that standard statistics used alone provide good classification results.

4.3 Other Features

Kerman [17], [41], [42] constructed a two-dimensional matrix of probabilities. Position (i, j) holds the probability that an intensity i has a neighbour j , where each pixel has eight adjoining neighbours. The probability $P(i, j)$ is estimated by counting the frequencies of occurrence $N(i, j)$ and dividing by the total number of bonds between i and each of its neighbours (usually eight bonds for every occurrence of intensity i).

In the example of Figure 4.6, for a 3×3 window, Kerman's probability vector is:

0	1	2
1	0	2
1	2	1

Figure 4.6: Image sample used to calculate the Kerman probability matrix.

$$P(0,0) = 2/11 = 0.18$$

$$P(0,1) = 6/11 = 0.55$$

$$P(0,2) = 3/11 = 0.27$$

$$P(1,1) = 4/16 = 0.25$$

$$P(1,2) = 6/16 = 0.38$$

$$P(2,2) = 4/13 = 0.31$$

Kerman plotted $P(i,j)$ versus j for every i with $j \geq i$ and discovered that the resulting plot was exponentially distributed. The exponential relationship is modeled by the equations in 4.1 and 4.2.

$$P(i,j) = \frac{1}{Q(i)} e^{-\beta(i) \times (i-j)}, i \geq j \quad (4.1)$$

$$-\ln(P(i,j)) = \beta(i) \times (i-j) + \ln(Q(i)), i \geq j \quad (4.2)$$

where $\beta(i)$ is the empirically determined slope of $-\ln(P(i,j))$ vs $(i-j)$, and $\ln(Q(i))$ is the empirically determined y-intercept of $-\ln(P(i,j))$ vs $(i-j)$.

Kerman proposes $\beta(i)$ and $\ln(Q(i))$ as features to aid in the separation of ice types in the image. $\beta(i)$ is a form of local textural information and $\ln(Q(i))$ is a measure of the spatial extent of the local textural information and is referred to as structural information.

The *Fourier Power Spectrum method (FPS)* [33] works in the frequency domain and describes spatial frequencies. Two common features used with the FPS are found by summing the spectrum contained in annular rings and in wedges. Features evaluated from rings measure texture coarseness, and features evaluated from wedge slices contain directionality information.

The Fourier Power Spectrum method is an expensive computational procedure and non-square regions present a problem with the evaluation of the transform [36]. Fourier spectrum provides global information such as directionality and average size but local information is sometimes lost in the frequency domain. Eklundh [43] found that phase information does not provide significant textural information. Connors *et al.* [44] and Weszka *et al.* [35] found that the performance of the Fourier spectrum method is significantly poorer than that of first and second order statistics.

The transform of the FPS is the *Autocorrelation Function (AF)* [33]. In a coarse texture where the primitives are large, the autocorrelation function will drop off slowly as the window is moved. A fine texture will yield an AF that drops off quickly.

The *Grey-Level Run Length Method (GLRL)* [45] measures the length of connected pixels having the same grey level. With the GLRL method, coarse textures are assumed to have many pixels in a constant grey tone run and smooth textures have few pixels in a constant grey tone run. The GLRL method suffers from noise sensitivity and the lack of grey level transition information [36].

4.4 Comparisons

A significant amount of research has been conducted in comparing the many feature extraction methods. The Grey-Level Co-occurrence Matrix is a very popular tool in sea ice classification, and thus it has been the focus of many comparative studies [44], [35], [24].

Conners and Harlow [44] and Weszka [35] performed studies on terrain samples to compare four textural feature procedures; second-order statistics (GLCM), first-order statistics (GLD), Fourier analysis (FPS), and grey-level run length (GLRL) method. Conners and Harlow ranked the above procedures from best to worst according to their performance: second-order statistics, first-order statistics, Fourier analysis, and Grey-Level Run Length method. Weszka *et al* reported similar results except that the second-order and first-order statistics performed equally well.

Although the GLCM is considered to perform very well, it suffers from two main difficulties. First, there is no established method of selecting values for a number of parameters such as displacement and window size. Second, a large number of features can be computed from the co-occurrence matrix, but there is no feature selection method to select the most relevant features.

Nystuen and Garcia [24] compared the performance of GLCM features and standard statistics in the classification of sea ice images. Their results show that standard statistics outperformed GLCM features in classifying sea ice images.

4.5 Summary

This chapter has provided an overview of many popular features. In Chapter 6, a number of features described in this chapter will be generated from the SAR sea

ice image. The features will then be used to assign costs to the links in the network so that an optimal path through the image can be found. The next chapter will describe a method of finding the optimal path between two points in a network.

Chapter 5

The Shortest Path Problem

Ship routes through ice fields are easily described in the language of networks, where a network is a collection of connected nodes. The nodes in the network correspond to individual pixels in a SAR image of the area and the links between the nodes are weighted according to some function of the ice at that location. The optimal path between the origin and the destination can be found by solving a well-known network optimization problem, the *shortest path problem*.

5.1 Network Definition

Every network is made up of nodes and links, and a cost, c_{ij} , that is associated with each link, (i, j) . In the sea ice network, the nodes are simply the $(row, column)$ coordinates of the sea ice image. Every node is linked to each of its eight neighbours (except when the node falls on an edge of the image). Each link, (i, j) , has an associated cost, c_{ij} , that reflects the ice conditions between node i and node j . Generally, if it is difficult for a ship to travel between node i and node j , then c_{ij}

must be large. Similarly, an easy passage between the two nodes will be indicated by a smaller c_{ij} .

5.2 Exhaustive Enumeration

Theoretically, the shortest path network problem can be solved simply by finding all possible routes, calculating each of their costs and choosing the best one. This is the technique of exhaustive enumeration. However, as the number of nodes increases, the number of possible routes increases exponentially. Thus, exhaustive enumeration is impractical as a means for solving the route network problem.

5.3 Dijkstra's Method

The shortest path problem is solved using the dynamic programming approach of Dijkstra [46]. Dijkstra's method divides the nodes in the network into those whose minimum-cost paths from node 1 have been identified (these are members of the *permanent set*), and all other nodes in the network (members of the *temporary set*). At every iteration, a new node is chosen from the temporary set and moved into the permanent set. The chosen node is always the one with the shortest path to the origin out of all the nodes in the temporary set.

Consider a network of nodes and links. The nodes are numbered from 1 to N . Each link (i, j) has associated with it a cost, c_{ij} , of traveling from node i to node j . Assume that $c_{ii} = 0$, but do not assume that the triangle inequality ($c_{ij} + c_{jk} \geq c_{ik}$) is satisfied. If there is no link between nodes i and j , then $c_{ij} = \infty$.

Let $P(j)$ represent the true shortest distance from node 1 to node j , where node j is a member of the *permanent* set. Let $T(k)$ represent the upper bound on the shortest distance from node 1 to node k , where the *temporary* value $T(k)$ may be updated in future iterations. Initially set $P(1) = 0$ and all other $T(i) = c_{1i}$, for $i \neq 1$.

Let PN represent the set of nodes that have permanent labels. Let TN represent the set of nodes that have temporary labels.

Initial conditions:

$$PN = [1]$$

$$TN = [2, 3, 4, 5, 6, 7, 8]$$

$$P(1) = 0$$

$$T(i) = c_{1i}, \text{ for all } i \notin PN.$$

Iterations:

1. Find node k from set TN such that $T(k) = \min_{i \notin PN} T(i)$.

$$\text{Set } P(k) = T(k).$$

$$PN = PN \cup [k] = [1, k].$$

2. If PN contains destination node N then STOP, else GOTO 3.

3. For each link (k, l) such that $l \notin PN$ (where k is from step 1),

$$T(l) = \min[T(l), P(k) + c_{kl}].$$

GOTO 1.

5.3.1 Example of Dijkstra's Algorithm

Figure 5.1 is used to demonstrate Dijkstra's algorithm. The shortest path from node 1 to node 8 is desired.

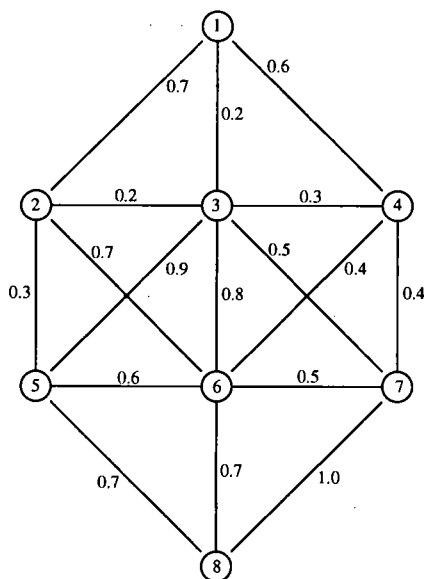


Figure 5.1: Network Example

Initial Conditions:

$$P(1) = 0$$

$$T(2) = 0.7, T(3) = 0.2, T(4) = 0.6, T(5) = \infty,$$

$$T(6) = \infty, T(7) = \infty, T(8) = \infty$$

Iteration 1: Node 3 has the smallest temporary label; node 3 is moved to the set of permanent nodes. At every iteration, each node's predecessor is updated. The predecessor of node 3 is node 1, that is, $B(3) = 1$.

$$P(1) = 0$$

$$\mathbf{P(3) = 0.2, B(3) = 1}$$

$$T(2) = \min[T(2), P(3) + c_{32}] = \min[0.7, 0.4] = 0.4, B(2) = 3$$

$$T(4) = \min[T(4), P(3) + c_{34}] = \min[0.6, 0.5] = 0.5, B(4) = 3$$

$$T(5) = \min[T(5), P(3) + c_{35}] = \min[\infty, 1.1] = 1.1, B(5) = 3$$

$$T(6) = \min[T(6), P(3) + c_{36}] = \min[\infty, 1.0] = 1.0, B(6) = 3$$

$$T(7) = \min[T(7), P(3) + c_{37}] = \min[\infty, 0.7] = 0.7, B(7) = 3$$

$$T(8) = \min[T(8), P(3) + c_{38}] = \min[\infty, \infty] = \infty$$

Iteration 2: Node 2 has the smallest temporary label.

$$P(1) = 0$$

$$P(3) = 0.2, B(3) = 1$$

$$P(2) = 0.4, B(2) = 3$$

$$T(4) = \min[T(4), P(2) + c_{24}] = \min[0.5, \infty] = 0.5, B(4) = 3$$

$$T(5) = \min[T(5), P(2) + c_{25}] = \min[1.1, 0.7] = 0.7, B(5) = 2$$

$$T(6) = \min[T(6), P(2) + c_{26}] = \min[1.0, 1.1] = 1.0, B(6) = 3$$

$$T(7) = \min[T(7), P(2) + c_{27}] = \min[0.7, \infty] = 0.7, B(7) = 3$$

$$T(8) = \min[T(8), P(2) + c_{28}] = \min[\infty, \infty] = \infty$$

Iteration 3: Node 4 has the smallest temporary label

$$P(1) = 0$$

$$P(2) = 0.4, B(2) = 3$$

$$P(3) = 0.2, B(3) = 1$$

$$P(4) = 0.5, B(4) = 3$$

$$T(5) = \min[T(5), P(4) + c_{45}] = \min[0.7, \infty] = 0.7, B(5) = 2$$

$$T(6) = \min[T(6), P(4) + c_{46}] = \min[1.0, 0.9] = 1.0, B(6) = 4$$

$$T(7) = \min[T(7), P(4) + c_{47}] = \min[0.7, 0.8] = 0.7, B(7) = 3$$

$$T(8) = \min[T(8), P(4) + c_{48}] = \min[\infty, \infty] = \infty$$

Iteration 4: Node 5 has the smallest temporary label.

$$P(1) = 0$$

$$P(2) = 0.4, B(2) = 3$$

$$P(3) = 0.2, B(3) = 1$$

$$P(4) = 0.5, B(4) = 3$$

$$\mathbf{P(5) = 0.7, B(5) = 2}$$

$$T(6) = \min[T(6), P(5) + c_{56}] = \min[0.9, 1.3] = 0.9, B(6) = 4$$

$$T(7) = \min[T(7), P(5) + c_{57}] = \min[0.7, \infty] = 0.7, B(7) = 3$$

$$T(8) = \min[T(8), P(5) + c_{58}] = \min[\infty, 1.4] = 1.4, B(8) = 5$$

Iteration 5: Node 7 has the smallest temporary label.

$$P(1) = 0$$

$$P(2) = 0.4, B(2) = 3$$

$$P(3) = 0.2, B(3) = 1$$

$$P(4) = 0.5, B(4) = 3$$

$$P(5) = 0.7, B(5) = 2$$

$$\mathbf{P(7) = 0.7, B(7) = 3}$$

$$T(6) = \min[T(6), P(7) + c_{76}] = \min[0.9, 1.2] = 0.9, B(6) = 4$$

$$T(8) = \min[T(8), P(7) + c_{78}] = \min[1.4, 1.7] = 1.4, B(8) = 5$$

Iteration 6: Node 6 has the smallest temporary label.

$$P(1) = 0$$

$$P(2) = 0.4, B(2) = 3$$

$$P(3) = 0.2, B(3) = 1$$

$$P(4) = 0.5, B(4) = 3$$

$$P(5) = 0.7, B(5) = 2$$

$$P(7) = 0.7, B(7) = 3$$

$$\mathbf{P(6) = 0.9, B(6) = 4}$$

$$T(8) = \min[T(8), P(6) + c_{68}] = \min[1.4, 1.6] = 1.4, B(8) = 5$$

Node 8 has the smallest temporary label and it is the end point.

$$P(1) = 0$$

$$P(2) = 0.4, B(2) = 3$$

$$P(3) = 0.2, B(3) = 1$$

$$P(4) = 0.5, B(4) = 3$$

$$P(5) = 0.7, B(5) = 2$$

$$P(6) = 0.9, B(6) = 4$$

$$P(7) = 0.7, B(7) = 3$$

$$P(8) = 1.4, B(8) = 5$$

The minimum cost path from node 1 to node 8 has a value of 1.4. To find the path, simply backtrack using the values in the B array.

$$B(8) = 5$$

$$B(5) = 2$$

$$B(2) = 3$$

$$B(3) = 1$$

Thus the shortest path is 1 - 3 - 2 - 5 - 8.

Note that the solution of the *simple path problem* by Dijkstra's method provides more than just the optimal path from node A to node N; the optimal path for node A to every node in the network is also included.

5.3.2 Proof of Dijkstra's Method

That Dijkstra's method finds the shortest path is proven inductively. At each iteration, k , of Dijkstra's procedure, the nodes are separated into two sets - the permanent (P) set and the temporary (T) set. The values of the nodes in set P are the true minimum distances from node 1. The values of the nodes in set T are

the shortest distances from node 1 that can be found using only the nodes in set P . To be proven is that the value of the smallest-valued node (i) in set T is the true minimum distance and can be transferred to set P . The statement is proven by noting that if a shorter path between node 1 and node i existed, it would have to include a node (j) that is in set T . However, a node in set T is necessarily farther from node 1 than is node i since node i has the smallest value in set T , and the path from node j to node i must have a non-negative length. Therefore, node i moves to set P . Node i is subsequently used to update the nodes in set T so that once again every node in set T has the smallest distance value possible using only the nodes in set P .

5.3.3 Computational Efficiency of Dijkstra's Method

The number of operations required by Dijkstra's procedure is calculated from the number of comparisons and additions at each iteration. There are $N - 1$ iterations, where N is the total number of nodes in the network. The first step in the procedure locates the smallest-valued node in the temporary set. If i is the iteration, then the number of comparisons is $N - 1 - i$. Next the members of set T are updated using $T(l) = \min[T(l), P(k) + c_{kl}]$, where l is a node in set T to be updated, k is the newest member of set P , and c_{kl} is the link cost between node k and node l . Here, $N - 1 - i$ comparisons and $N - 1 - i$ additions are performed. In addition, each node in the network is marked 'permanent' or 'temporary' by an attached index number which changes from 0 to 1 when the node moves to the permanent set. Thus at every iteration i , each node's index number has to be consulted (except for node 1) at a cost of $N - 1$ comparisons. The number of comparisons is $(N - 1)^2 + 2 \sum_{i=1}^{N-1} (N - 1 - i) = 3(N - 1)^2 - N(N - 1) = (N - 1)(2N) \approx 2N^2$. The number of additions is $\sum_{i=1}^{N-1} (N - 1 - i) = (N - 1)^2 - N(N - 1)/2 \approx N^2/2$.

Thus the total number of operations is on the order of N^2 .

5.4 Modifications to Dijkstra's Procedure

I modified Dijkstra's algorithm to include an ordered linked list that stores the temporary nodes and values. LL represents the linked list and the list entry $[i, T(i)]$ represents node i and a temporary value of $T(i)$.

Initial conditions:

$$P(1)=0.$$

$$T(i)=\infty, \text{ for all temporary } i.$$

$$LL = [(1, 0)].$$

Iterations:

1. Find node k from LL such that value $T(k)$ is minimum.
2. If k is destination node N then STOP, else GOTO 3.
3. For each link (k, l) such that l is a temporary-valued neighbour of k (where k is from step 1),

$$T(l) = \min[T(l), P(k) + c_{kl}].$$
 Add each $[l, T(l)]$ to LL in the order of highest to lowest $T(l)$.
 Move $T(k)$ to permanent set: $P(k) = T(k)$.
 Remove $P(k)$ from LL .
 GOTO 1.

5.4.1 Benefits of Modifications

At every iteration, Dijkstra's method requires that the smallest-valued node in the temporary set is located. The temporary set includes all nodes that are not in the permanent set including those with a value of ∞ . For example, at the first iteration, node 1 is in the P set and all other nodes are in the T set. All nodes in the T set except for a maximum of eight nodes will have a value of infinity. Dijkstra's algorithm checks through all $N - 1$ nodes to find the minimum. In the modified version, the linked-list contains the ordered nodes of the temporary set (with values $< \infty$). The smallest-valued node is at the end of the list so that no search is required. Next, if k is the newest addition to the permanent set, every node l in the temporary set is updated according to $T(l) = \min[T(l), P(k) + c_{kl}]$. In Dijkstra's method, a comparison and addition is made for every member l of the temporary set even those that are not linked to k (where $c_{kl} = \infty$). In the modified algorithm, only the immediate neighbours, if they are members of the temporary set, are modified for a maximum of 8 comparisons and 8 additions.

5.4.2 Example of Modified Algorithm

Figure 5.1 is again used to demonstrate Dijkstra's algorithm. The shortest path is desired from node 1 to node 8.

Initial Conditions:

$$P(1) = 0$$

$$T(2) = T(3) = T(4) = T(5) = T(6) = T(7) = T(8) = \infty$$

$$LL = [(1, 0)]$$

Iteration 1: The temporary neighbours of node 1 = [2, 3, 4].

$$P(1) = 0$$

$$T(2) = \min[T(2), P(1) + c_{12}] = \min[\infty, 0.7] = 0.7, B(2) = 1$$

$$T(3) = \min[T(3), P(1) + c_{13}] = \min[\infty, 0.2] = 0.2, B(3) = 1$$

$$T(4) = \min[T(4), P(1) + c_{14}] = \min[\infty, 0.6] = 0.6, B(4) = 1$$

- Add $T(2)$, $T(3)$, and $T(4)$ to LL in order of highest to lowest cost, c .
- Remove $P(1)$ from LL.

$$LL = [(2, 0.7), (4, 0.6), (3, 0.2)]$$

Iteration 2: Node 3 has the smallest temporary value in LL. The temporary neighbours of node 3 = [2, 4, 5, 6, 7].

$$P(1) = 0$$

$$P(3) = 0.2, B(3) = 1$$

$$T(2) = \min[T(2), P(3) + c_{32}] = \min[0.7, 0.4] = 0.4, B(2) = 3$$

$$T(4) = \min[T(4), P(3) + c_{34}] = \min[0.6, 0.5] = 0.5, B(4) = 3$$

$$T(5) = \min[T(5), P(3) + c_{35}] = \min[\infty, 1.1] = 1.1, B(5) = 3$$

$$T(6) = \min[T(6), P(3) + c_{36}] = \min[\infty, 1.0] = 1.0, B(6) = 3$$

$$T(7) = \min[T(7), P(3) + c_{37}] = \min[\infty, 0.7] = 0.7, B(7) = 3$$

- Update $T(2)$ and $T(4)$ in LL.
- Add $T(5)$, $T(6)$, and $T(7)$ to LL.
- Remove $P(3)$ from LL.

$$LL = [(5, 1.1), (6, 1.0), (7, 0.7), (4, 0.5), (2, 0.4)]$$

Iteration 3: Node 2 has the smallest temporary value in LL. The temporary neighbours of node 2 = [5, 6].

$$P(1) = 0$$

$$P(3) = 0.2, B(3) = 1$$

$$P(2) = 0.4, B(2) = 3$$

$$T(5) = \min[T(5), P(2) + c_{25}] = \min[1.1, 0.7] = 0.7, B(5) = 2$$

$$T(6) = \min[T(6), P(2) + c_{26}] = \min[1.0, 1.1] = 1.0, B(6) = 3$$

- Update $T(5)$ from LL.
- Remove $P(2)$ from LL.

$$LL = [(6, 1.0), (7, 0.7), (5, 0.7), (4, 0.5)]$$

Iteration 4: Node 4 has the smallest temporary value in LL. The temporary neighbours of node 4 = [6, 7].

$$P(1) = 0$$

$$P(2) = 0.4, B(2) = 3$$

$$P(3) = 0.2, B(3) = 1$$

$$P(4) = 0.5, B(4) = 3$$

$$T(6) = \min[T(6), P(4) + c_{46}] = \min[1.0, 0.9] = 0.9, B(6) = 4$$

$$T(7) = \min[T(7), P(4) + c_{47}] = \min[0.7, 0.9] = 0.7, B(7) = 3$$

- Update $T(6)$ from LL.
- Remove $P(4)$ from LL.

$$LL = [(6, 0.9), (7, 0.7), (5, 0.7)]$$

Iteration 5: Node 5 has the smallest temporary value in LL. The temporary neighbours of node 5 = [6, 8].

$$P(1) = 0$$

$$P(2) = 0.4, B(2) = 3$$

$$P(3) = 0.2, B(3) = 1$$

$$P(4) = 0.5, B(4) = 3$$

$$P(5) = 0.7, B(5) = 2$$

$$T(6) = \min[T(6), P(5) + c_{56}] = \min[0.9, 1.3] = 0.9, B(6) = 4$$

$$T(8) = \min[T(8), P(5) + c_{58}] = \min[\infty, 1.4] = 1.4, B(8) = 5$$

o Add $T(8)$ to LL.

o Remove $P(5)$ from LL.

$$LL = [(8, 1.4), (6, 0.9), (7, 0.7)]$$

Iteration 6: Node 7 has the smallest temporary value in LL. The temporary neighbours of node 7 = [6, 8].

$$P(1) = 0$$

$$P(2) = 0.4, B(2) = 3$$

$$P(3) = 0.2, B(3) = 1$$

$$P(4) = 0.5, B(4) = 3$$

$$P(5) = 0.7, B(5) = 2$$

$$P(7) = 0.7, B(7) = 3$$

$$T(6) = \min[T(6), P(7) + c_{76}] = \min[0.9, 1.2] = 0.9, B(6) = 4$$

$$T(8) = \min[T(8), P(7) + c_{78}] = \min[1.4, 1.7] = 1.4, B(8) = 5$$

o Remove $P(7)$ from LL.

$$LL = [(8, 1.4), (6, 0.9)]$$

Iteration 7: Node 6 has the smallest temporary value in LL. The temporary neighbours of node 6 = [8].

$$P(1) = 0$$

$$P(2) = 0.4, B(2) = 3$$

$$P(3) = 0.2, B(3) = 1$$

$$P(4) = 0.5, B(4) = 3$$

$$P(5) = 0.7, B(5) = 2$$

$$P(7) = 0.7, B(7) = 3$$

$$P(6) = 0.9, B(6) = 4$$

$$T(8) = \min[T(8), P(6) + c_{68}] = \min[1.4, 1.6] = 1.4, B(8) = 5$$

o Remove $P(6)$ from LL.

$$LL = [(8, 1.4)]$$

Iteration 8: Node 8 has the smallest temporary value in LL. Node 8 is the end point.

$$P(1) = 0$$

$$P(2) = 0.4, B(2) = 3$$

$$P(3) = 0.2, B(3) = 1$$

$$P(4) = 0.5, B(4) = 3$$

$$P(5) = 0.7, B(5) = 2$$

$$P(6) = 0.9, B(6) = 4$$

$$P(7) = 0.7, B(7) = 3$$

$$P(8) = 1.4, B(8) = 5$$

Thus the shortest path is $8 - 5 - 2 - 3 - 1$.

5.5 Summary

This chapter has outlined a method of finding an optimal path through a network. The SAR image is the network and the pixels in the image are the nodes of the

network. Each pair of nodes is joined by a link. The costs associated with each link corresponds to the difficulty faced by a vessel when traversing that particular section of water. In the next chapter, a method of calculating the link costs based on the features extracted in Chapter 4 is presented.

Chapter 6

Cost Assignment

The previous chapter discussed Dijkstra's method for finding the minimum-cost path through a network. The nodes of the network are the pixels in the SAR sea ice image and the link costs represent the difficulty experienced by a vessel while traveling along the link. The costs may be related to the ice properties such as ice strength or thickness, or may focus on the ship's costs such as the transit time, the amount of fuel consumed, or the risk of damage. In this Chapter, costs measured from the ice properties will be minimized; ship-related costs are the focus of Chapter 7.

Features, such as standard deviation and Haralick's features, are often used for classifying ice in a SAR image. In the first part of this section, several commonly used features will be tested for their ability to separate the three ice types. The successful ones will be used to assign meaningful link costs. The lowest-cost path will then be selected using Dijkstra's network technique. In the second part of this section, the network links will be assigned costs based on Kerman's bonding probability.

6.1 Methodology

Here, the image features to be used in the cost assignment are selected. The best features clearly separate the three ice types. Four cost functions will be formed for each of the features selected. A cost function, $c(x)$ uses a feature image to assign costs to each intensity in the image. Routes for three sets of starting and ending points will be used to compare the performance of the image features and cost functions.

6.1.1 Selection of Features

Of the features introduced in Chapter 4, only four feature groups are selected: tone, standard deviation, Weszka's first-order entropy, and mean features, and Haralick's second-order contrast and entropy features. These features successfully separate the three ice types in the image. Tone, standard deviation, and Haralick's features are commonly used for classification purposes [21]. Weszka's features are not as popular but two studies have found them to perform as well as Haralick's features [44, 35].

Generation of Histograms

The SAR sea ice image is classified into regions of lead, first-year, and multi-year ice. Many unsupervised classification approaches are available but for simplicity, a rough, manual technique is used. Several training regions corresponding to each of the three ice types are defined and three histograms are generated. Each histogram is normalized by first dividing by the number of pixels in the respective training area and then multiplying by the estimated number of pixels of the appropriate ice type in the image. For the C-band image (Figure 3.2), the estimated ratio of lead

to first-year to multi-year ice is 1 : 12 : 7.

Description of Histograms

Figure 6.1 displays well-separated histograms of the tone feature. Although there is overlap in intensity between the three ice types, in general, as the intensity increases, the age of the ice increases, and the older the ice, the thicker and stronger it is. Figures 6.2 – 6.6 are the histograms for the texture features. These histograms are fairly well separated and therefore can be used to distinguish between the three ice types. There is generally some overlap between the first-year ice histogram and the multi-year ice histogram. This occurs because the first-year ice training set includes first-year rubble ice whose texture, like that of multi-year ice, is very rough.

A requirement of the selected features is that lead ice is darker than first-year ice, which in turn is darker than multi-year ice. Therefore, the lead histogram is on the left, followed by the first-year ice histogram, and then the multi-year ice histogram.

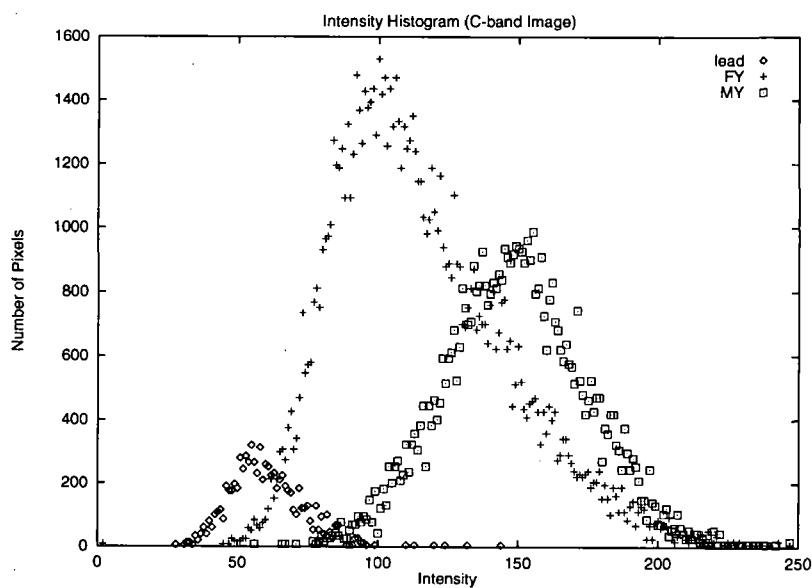


Figure 6.1: Intensity histograms for 3 ice types.

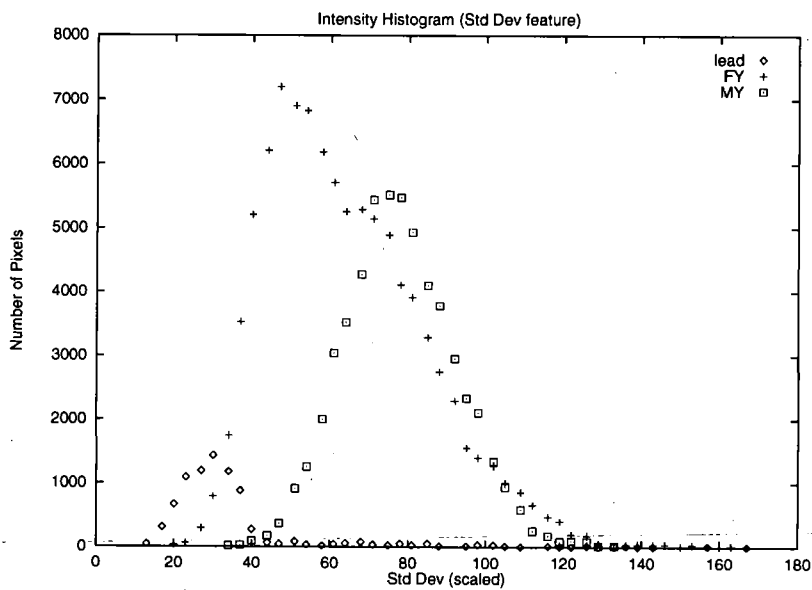


Figure 6.2: Standard Deviation histograms for 3 ice types.

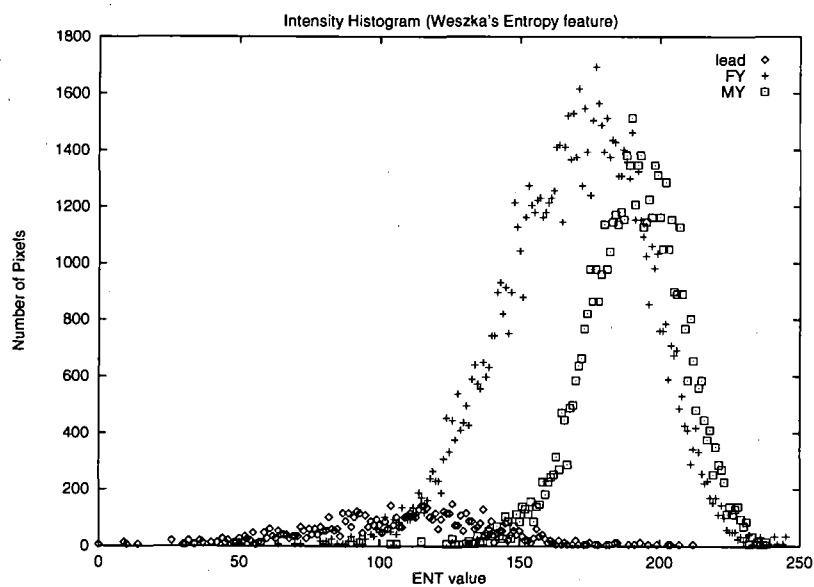


Figure 6.3: Weszka's Entropy feature histograms for 3 ice types.

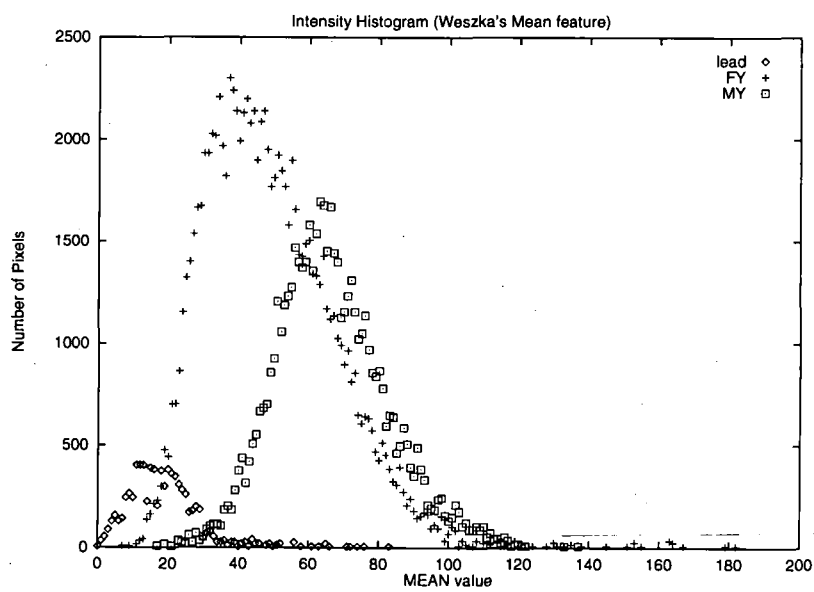


Figure 6.4: Weszka's Mean feature histograms for 3 ice types.

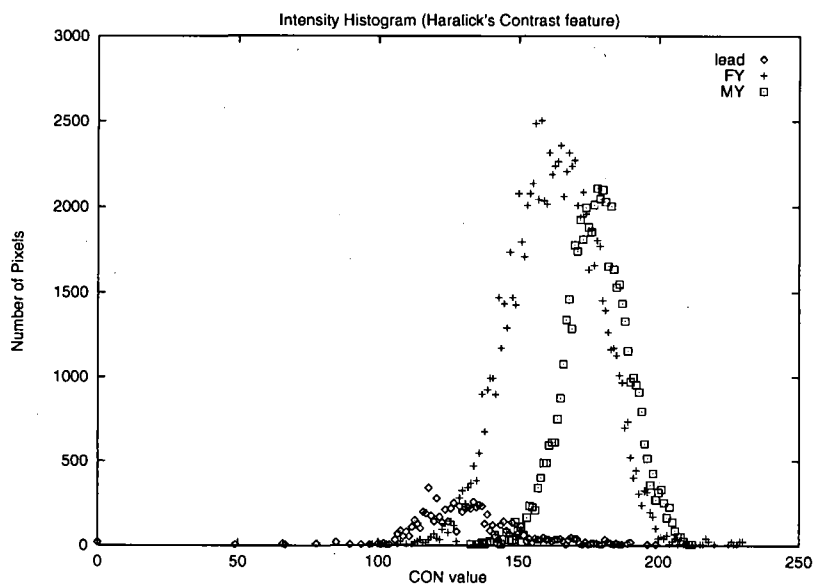


Figure 6.5: Haralick's Contrast feature histograms for 3 ice types.

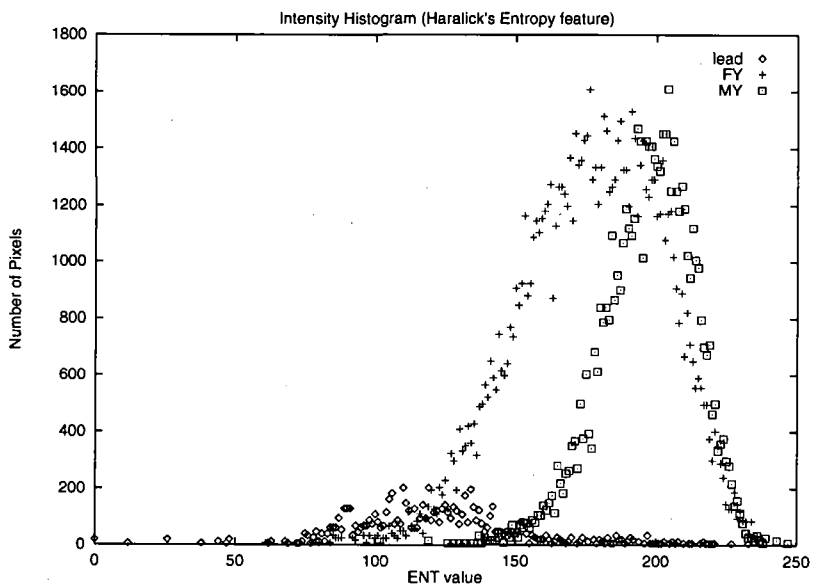


Figure 6.6: Haralick's Entropy feature histograms for 3 ice types.

Generation of Features

Tone Feature: The tone feature is simply the C-band image (Figure 3.2).

Standard Deviation Feature: Figure 6.7 is the standard deviation image of the C-band image (Figure 3.2). A 5×5 local window was used.

Weszka's Grey Level Dependence Matrix Features: Two of Weszka's [35] texture features, entropy and mean, are shown in Figures 6.8 and 6.9. A 5×5 local window is used. $\delta = 1$ and all eight neighbours are used simultaneously.

Haralick's Grey-Level Co-occurrence Matrix Features: Two of Haralick's second-order texture features [39], entropy and contrast, are generated from the C-band image. The number of grey levels is 16 so that the GLC matrices are 16×16 . The local window is 5×5 , the distance is 1, and all eight neighbours are used simultaneously. The logarithm of the contrast feature is displayed because of the poor contrast in the original.

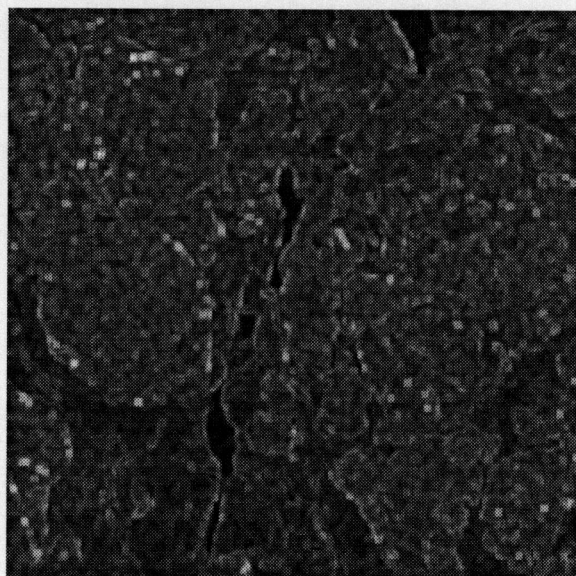


Figure 6.7: Standard Deviation image of SAR image.

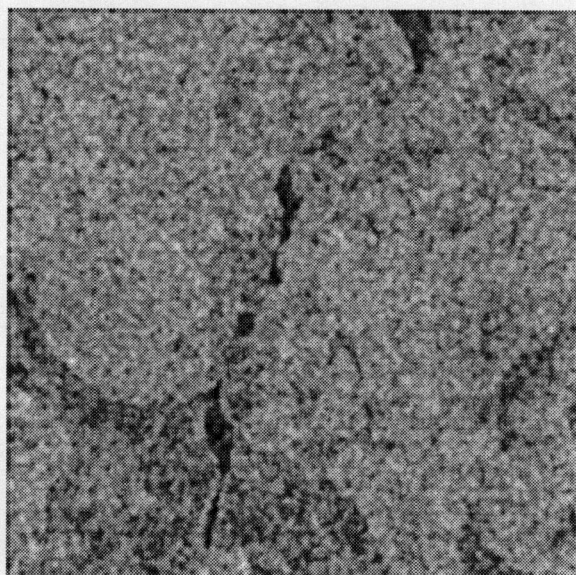


Figure 6.8: Weszka's Entropy feature.

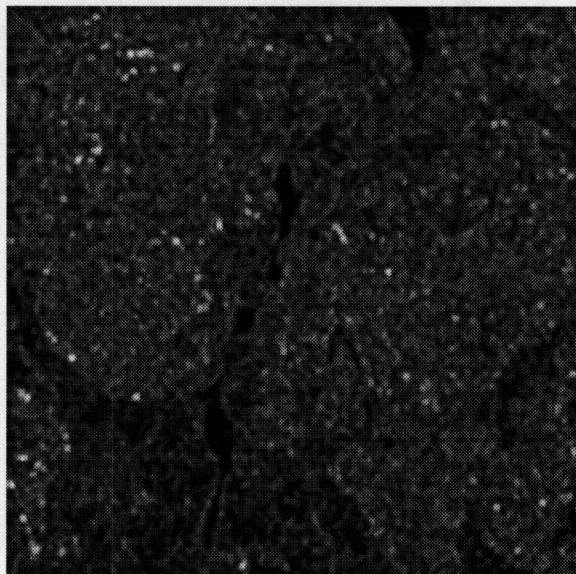


Figure 6.9: Weszka's Mean feature.

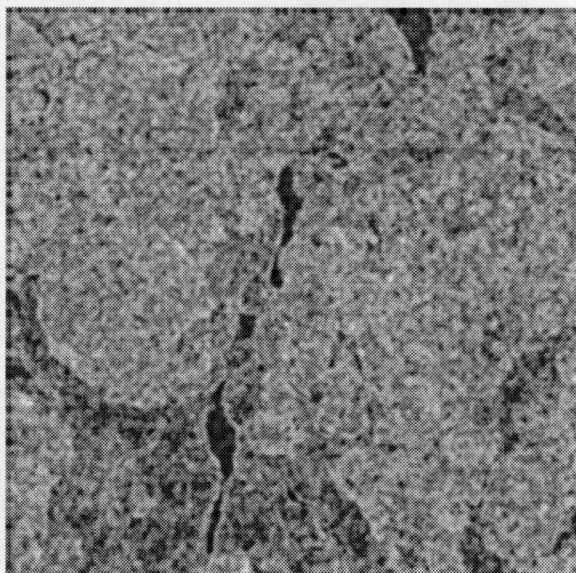


Figure 6.10: Haralick's Entropy feature.

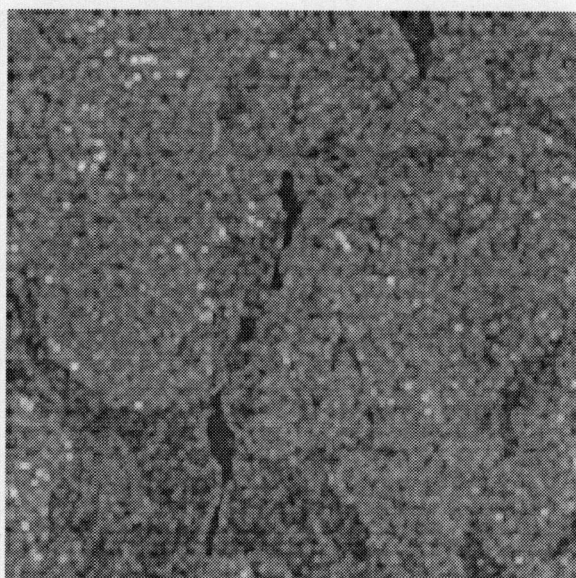


Figure 6.11: Haralick's Contrast feature.

6.1.2 Selection of Routes

Three sets of starting and ending points are used as input. Routes are generated using all combinations of cost functions and features. Table 6.1 lists the three sets of end-points and Figure 6.12 displays their position on the C-band image. For the first set of end-points, the optimal route follows the dark lead the entire way. The second set of end-points requires the route to follow the dark lead and then make a detour near the destination point. The third set of end-points are far from the lead. However, the straight line connecting the end-points passes through first-year rubble and dangerous multi-year ice floes. The optimal path crosses over to the lead and follows it until making a detour to the destination point.

Table 6.1: End-Points

Start (row,col)	End (row,col)
1: (0,275)	1': (399,99)
2: (0,275)	2': (399,253)
3: (95,399)	3': (399,253)

6.1.3 Selection of Cost Functions

Four cost functions are explored: the threshold cost function, the probability weighted cost function, the linear cost function, and the quartic cost function. A cost function is expressed as $c(x)$, where x is determined by the feature. The cost functions are illustrated using the tone feature image (Figure 3.2).

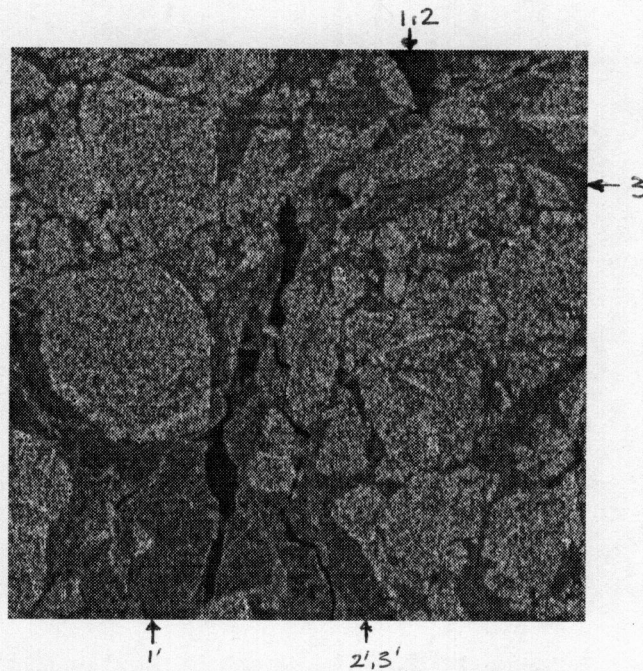


Figure 6.12: End-points of the three paths.

Threshold Cost Function

Using Figure 6.1, two tonal thresholds can be found; one that separates easy lead ice from more difficult first-year ice, and one that separates first-year ice from very difficult multi-year ice. The thresholds are estimated at intensities 64 and 134. Next, the penalty attributed to each ice type is assigned. The penalty represents the difficulty experienced by a ship in crossing through the particular ice type. Penalties are assigned to the three ice types: 0.01 to lead ice, 0.1 to first-year ice, and 1.0 to multi-year ice. Therefore, it is 10 times more difficult to travel through first-year ice than lead ice, and it is 100 times more difficult to travel through multi-year ice than lead ice. The penalty functions were arbitrarily separated by a factor of 10. Lead ice is assigned the smallest penalty because it offers the least resistance to ships, and multi-year ice has the largest penalty because ships have

great difficulty in passing through it. The threshold cost function is:

$$c(x) = \begin{cases} 0.01 & x \leq 64 \\ 0.1 & 65 < x < 134 \\ 1.0 & x \geq 135 \end{cases}$$

The thresholds are located at the intersection between two histograms. Table 6.2 lists the thresholds for all six features. The first threshold is that which separates lead ice from first-year ice and the second threshold separates first-year ice from multi-year ice.

Table 6.2: Thresholds

Features	Thresholds	
Tone	64	134
Std Dev	34	71
Weszka's Entropy	113	190
Weszka's Mean	20	60
Haralick's Entropy	122	200
Haralick's Contrast	130	172

Distance traveled must also be minimized. When minimizing with Dijkstra's procedure, the cost of a diagonal link is multiplied by $\sqrt{2}$ to adjust for the longer distance. Therefore, the cost of the link (i, j) is equal to the distance between i and j ($\sqrt{2}$ or 1) multiplied by $c(j)$.

Four shortcomings are apparent with the threshold cost function: (i) the image must be segmented into the three ice types, (ii) the penalties assigned to each ice type are arbitrary, (iii) each intensity within an ice type is treated equally even though some first-year ice is easier to traverse than other first-year ice, and (iv) a

pixel with an intensity belonging to one ice type might be mis-classified as a different ice type.

Probability Weighted Cost Function

The performance of each feature may be further studied by plotting the probability of ice-type versus intensity. Figure 6.13 is the corresponding plot for the tone feature. In this figure, it is clear that all pixels with an intensity of less than 48 belong to lead ice. Pixels with an intensity of 100 have a 95 percent chance of being first-year ice and a 5 percent chance of being multi-year ice.

A pixel's link cost is calculated by summing the multiplication of ice-type probability with ice-type penalty for each ice-type, then adjusting for distance. The ice-type penalties are the same as those of Section 6.1.3: 0.01, 0.1, and 1.0 for lead, first-year, and multi-year ice respectively. The cost function is:

$$c(x) = 0.01P(\text{lead}|x) + 0.1P(\text{fy}|x) + 1.0P(\text{my}|x)$$

$P(\text{lead}|x)$ is the probability that pixel x is lead ice, $P(\text{fy})$ is the probability that pixel x is first-year ice, and $P(\text{my})$ is the probability that pixel x is multi-year ice.

Two shortcomings of the probability weighted cost function are (i) the image must be segmented, and (ii) the ice-type penalties were chosen arbitrarily.

Linear Cost Function

If a segmented image is not available, the previous two methods are not useful. However, a route can still be found. In such a case, two relationships are important: that between ice thickness and tone, and that between ice thickness and texture. Figure 6.1 shows that the tonal intensity tends to increase with increasing

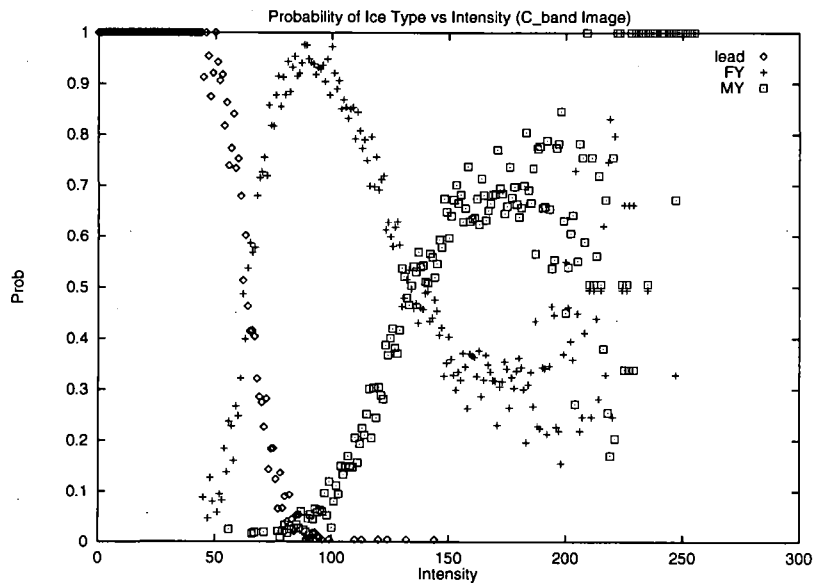


Figure 6.13: Probability of ice type, tonal feature.

ice age, and ice thickness is correlated with ice age. Figures 6.2 – 6.6 show that the intensity of textural features also increases with increasing ice thickness. Thus, a cost function can be defined where the cost is linearly dependent with tone or texture.

The linear cost function is $c(x) = \frac{I}{\max(I)}$, where x is intensity and $\max(x)$ is the maximum intensity value in the image, and where the image can be any tonal or textural feature.

Quartic Cost Function

The cost function can also be non-linear with intensity; a quartic function is chosen. The quartic function is $c(x) = (\frac{x}{\max(x)})^4$, where x is intensity and $\max(x)$ is the maximum intensity value in the image.

The power of 4 is not completely arbitrary. In an idealized image, the two

thresholds of the three ice-type histograms are exactly $\frac{\max(I)}{3}$, and $\frac{2\max(I)}{3}$. The penalty values at the two thresholds and at $\max(I)$ are 0.012, 0.2, and 1.0 respectively. These numbers correspond very well to the ice-type penalties of Section 6.1.3.

A shortcoming of the quartic cost function approach is that it is not based on any underlying physical properties of the image. The power of 4 was chosen by intuitive means not through measurement, and may not produce similar good results with other images. The quartic cost function is just an example of a non-linear cost function. Any arbitrary $c(x)$ can be created.

6.2 Results

Figures 6.14, 6.15, and 6.16 display the three routes selected using the tonal feature Figure 3.2 and the threshold-based cost function. All three paths appear optimal. The paths tend to follow the dark leads as much as possible while still trying to minimize the distance traveled.

Table 6.3 evaluates the three resulting paths generated by the minimization of each of the 24 combinations of features and cost functions. An entry is marked 'Good' if the resulting paths are similar to those of Figures 6.14 – 6.16. Any significant deviations from the 'Good' paths are classed as 'Poor'. Two examples of 'Poor' paths follow in Figures 6.17 – 6.18.

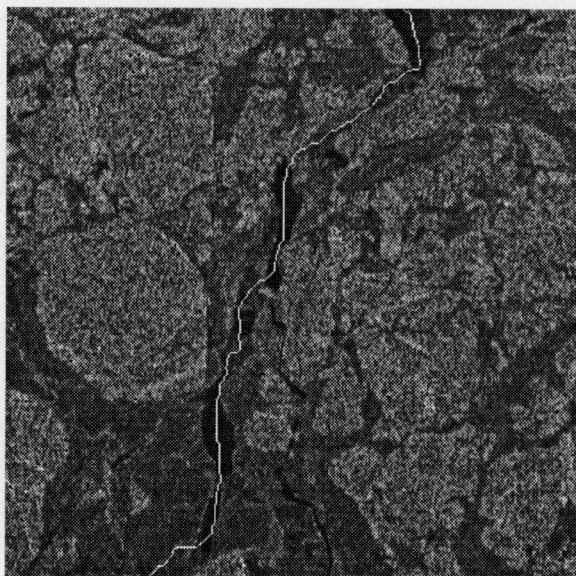


Figure 6.14: Path 1 using tone feature and threshold cost function.

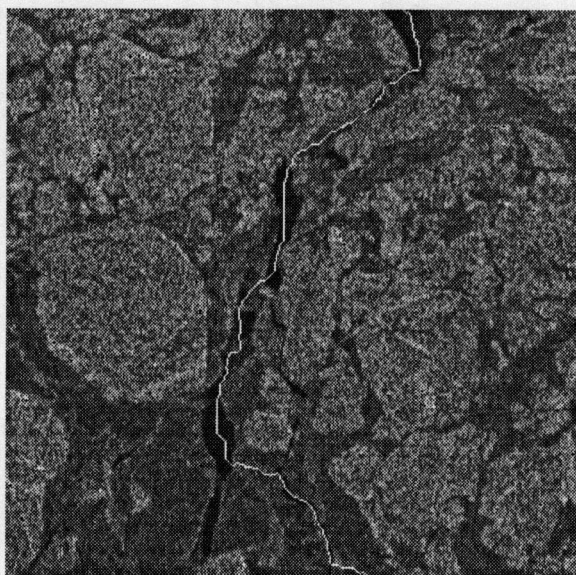


Figure 6.15: Path 2 using tone feature and threshold cost function.

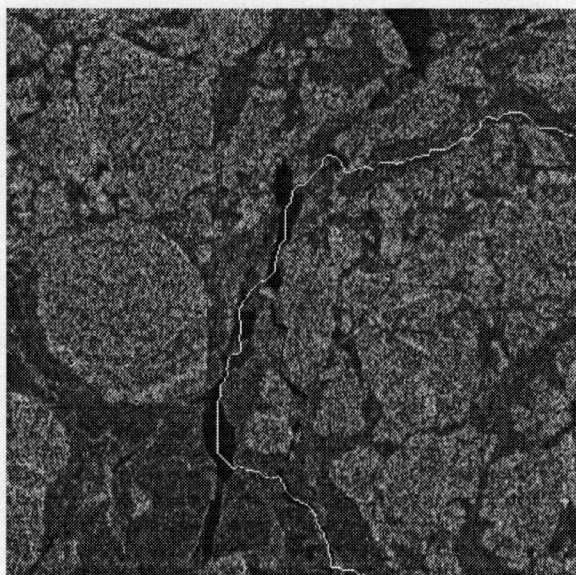


Figure 6.16: Path 3 using tone feature and threshold cost function.

Table 6.3: Summary of Results

Features		Cost Functions			
		Threshold Function	Weighted Probability	Linear Function	Quartic Function
<i>Tone</i>	Route 1	Good	Good	Good	Good
	2	Good	Good	Good	Good
	3	Good	Good	Poor	Good
<i>Standard Deviation</i>	Route 1	Good	Good	Good	Good
	2	Good	Good	Good	Good
	3	Poor	Poor	Poor	Good
<i>Weszka Entropy</i>	Route 1	Good	Good	Good	Good
	2	Good	Poor	Good	Good
	3	Poor	Good	Poor	Good
<i>Weszka Mean</i>	Route 1	Good	Good	Good	Good
	2	Good	Good	Good	Good
	3	Good	Good	Poor	Good
<i>Haralick Entropy</i>	Route 1	Good	Good	Poor	Good
	2	Good	Good	Poor	Good
	3	Poor	Good	Poor	Good
<i>Haralick Contrast</i>	Route 1	Good	Good	Poor	Good
	2	Good	Good	Poor	Good
	3	Good	Good	Poor	Poor

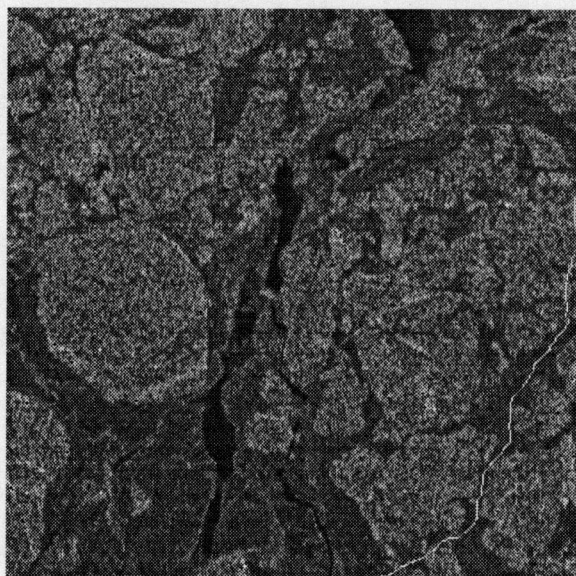


Figure 6.17: Path 3 using Tone feature and Linear cost function.

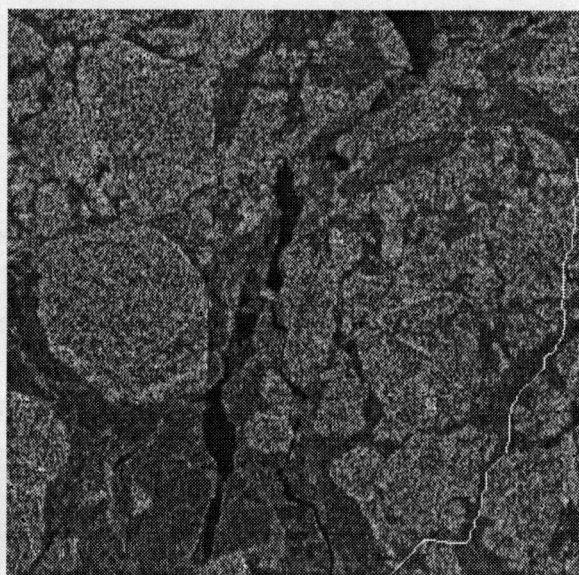


Figure 6.18: Path 3 using Haralick's Contrast feature and Quartic cost function.

6.3 Cost Assignment using Kerman's Exponential Relationship

As stated in Chapter 4, Kerman [17] found that for a SAR sea-ice image, the joint probability of intensity i and neighbouring pixel intensity j is exponentially distributed such that:

$$P(i, j) = \frac{1}{Q_i} e^{-\beta_i \times (i-j)}, i \geq j \quad (6.1)$$

β_i and Q_i are both empirically determined and are unique for different values of i .

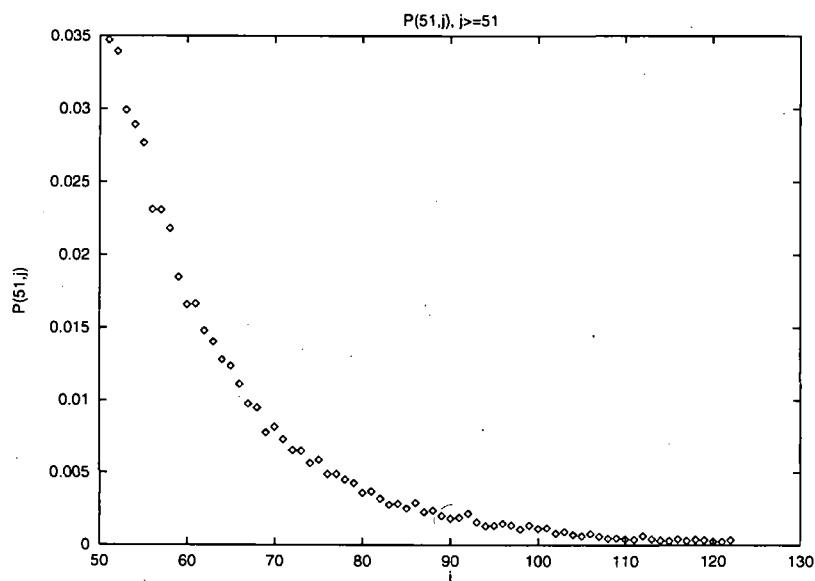
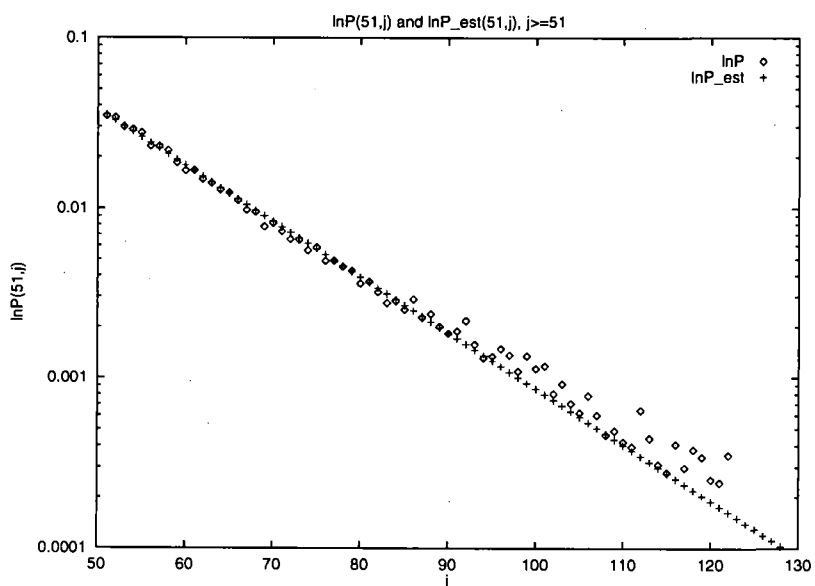
Since the joint probability $P(i, j)$ found for the C-band image (Figure 3.2) is not clearly exponential, the L-band image (Figure 3.1) will be used. The L-band image produced an excellent exponential joint probability distribution. Figure 6.19 is the joint probability distribution for $i = 51$, the intensity at which the cumulative probability function equals 50 percent. Figure 6.20 illustrates the exponential characteristic of the distribution by overlaying the logarithm of the joint probability distribution with a straight line, P_{est} .

Kerman also defines a bonding probability ([42]) according to Equation 6.2. Note that the equation for bonding probability is similar to that of the joint probability with the exception of the scaling factor, Q_i .

$$P_b(i, j) = \exp(-\beta(i) \times (j - i)), j \geq i \quad (6.2)$$

The bonding probability between two adjoining pixels expresses the likelihood that the two pixels belong to the same material. If $P(i, j)$ is large, the bonding probability between i and j is also large because neighbouring pixels with these intensities likely belong to the same ice type.

The bonding probability can be used to assign costs to the links in the network. An important assumption must first be made: if a particular pair of intensities,

Figure 6.19: Joint probability distribution, $P(51, j)$ Figure 6.20: Logarithm of $P(51, j)$ and the exponential overlay P_{est}

(i, j) , occurs frequently through the image (that is, $P(i, j)$ is large), then the presence of i, j pairs signals the location of an ice type. Similarly, if $P(i, j)$ is small, then it suggests either that the occurrence of the intensity pair is due to a noise element, or that the combination occurs along a border of two ice types.

The larger the bonding probability, $P_b(i, j)$, between two adjacent pixels, the more likely it is that the two pixels belong to the same ice type. In other words, if a pixel of intensity i belongs to ice type a , and $P_b(i, j)$ is large, then a neighbouring pixel of intensity j likely belongs to ice type a . We can construct a path through the ice by knowing the bonding probability between neighbouring pixels. The starting point of the path must belong to a navigable ice type such as lead ice. A cost is assigned to each link in the network. Since the bonding probability needs to be maximized, the costs assigned to the links are inversely related to the bonding probability. The link costs are assigned the value of $1 - P_b(i, j)$.

A shortcoming of the bonding probability cost function is that the bonding probability is large between two intensities that occur frequently regardless of the ice type. Thus, two frequently occurring neighbouring intensities within difficult multi-year ice will exhibit high bonding probability. If the path is able to break through an ice-type boundary into difficult ice, the high bonding probabilities will suggest a path through difficult ice. There is no way to determine the ice type with the bonding probability alone. This method can be improved by incorporating the use of a segmented image of ice type.

6.3.1 Results

Figures 6.21, 6.22, and 6.23 illustrate the three paths that are generated using Kerman's bonding probability. Paths 1 and 2 appear optimal, however, Path 3

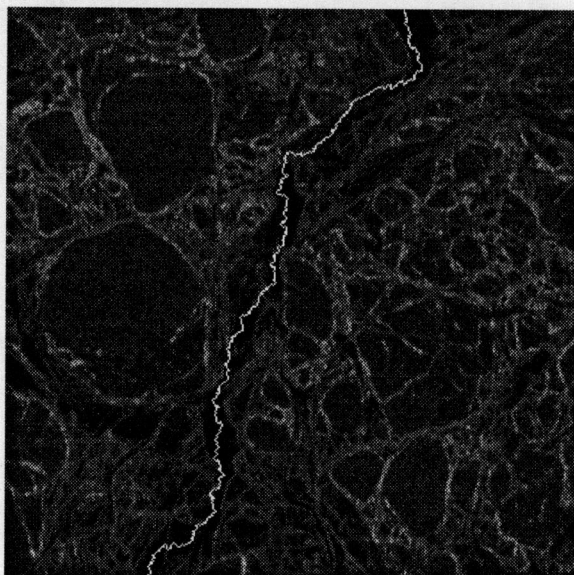


Figure 6.21: Path 1 using Kerman's bonding probability.

passes through difficult ice.

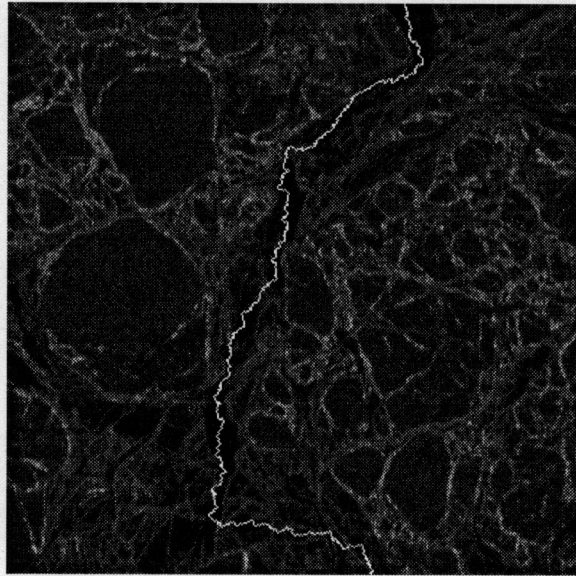


Figure 6.22: Path 2 using Kerman's bonding probability.

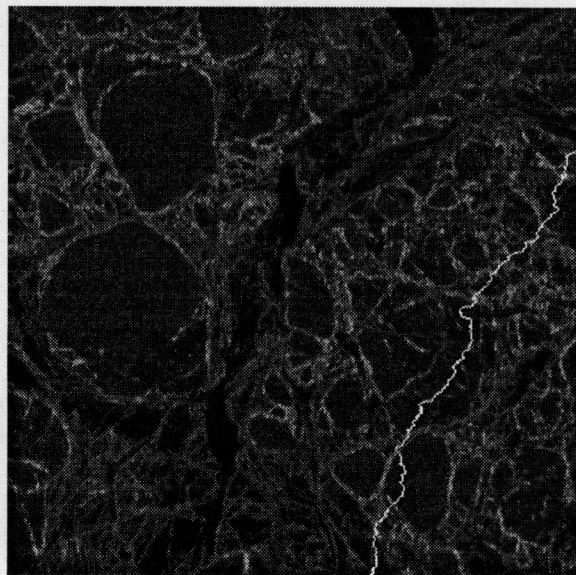


Figure 6.23: Path 3 using Kerman's bonding probability.

6.4 Conclusions

The threshold function and the weighted probability function perform very well.

In general, the linear cost function performed poorly for all features. The histograms of the feature images (Figures 6.1 – 6.5) show that there is only a small separation between the three ice types. It is necessary for the cost function to further separate the ice types. The linear cost function provides no further separation and thus it performs poorly. The improved performance of the quartic cost function is due to its success in separating the ice types.

Link costs based on Kerman's bonding probability produced two paths that were quite good. The third path passed through difficult ice.

The two features that performed the best overall were tone and Weszka's mean feature.

Chapter 7

Vessel Performance

In previous chapters, the SAR sea ice image was manipulated mathematically to give information about the ice conditions. Chapter 6 used this ice information to calculate cost values for the links in the image network. The costs were not translated into measures of a vessel's performance.

In trying to quantify a vessel's performance along an ice-covered route, the interaction between the vessel and the surrounding ice must be understood. A vessel is described by its physical dimensions (beam, draft, length), angular geometry (hull bow angles), and propulsion system. The surrounding ice is represented by its thickness. This chapter proposes a method for calculating the transit time of a vessel as a means of determining the vessel's performance. Optimal routes can then be generated automatically by minimizing the transit time.

The transit time over a route is calculated from the vessel's velocity, where the velocity is dependent on the encountered ice resistance and the strength of the vessel. A number of experimentally-developed formulae dealing with the resistance of continuous ice are available in the literature [47, 48, 49, 50]. Continuous ice has

an ice coverage of 100% and no ridges are present. Continuous ice resistance is a function of vessel speed, ice thickness, material constants, and vessel configuration parameters.

Table 7.5, at the end of this chapter, lists the notation used.

7.1 Ice Resistance

One of the earliest efforts to calculate the ice resistance on a moving vessel is that of Kashteljan *et al.* [50]. Kashteljan separated total ice resistance into three main components: (i) R_B , the resistance due to the breaking of the ice, (ii) R_S , the resistance due to the turning and submerging of the ice, and (iii) R_V , the velocity-dependent resistance. Many ice resistance formulae have been developed from Kashteljan's work. The basic icebreaking physics is not well understood, so most ice resistance formulae are empirical in nature and use various indices and coefficients determined experimentally. There is considerable disagreement between the various ice resistance formulae concerning the exact relationships between resistance and ice thickness, and resistance and ship velocity. In selecting a suitable equation, two criteria were considered; the equation should consider all ship and ice parameters that are known to affect the resistance, and the equation should keep empirical constants to a minimum. In this report, Enkvist's [49] formulation (Equation 7.1) was chosen to calculate the ice resistance as a function of thickness (h) and velocity (v) for movement in continuous ice:

$$R(h, v) = (C_1 h + C_2) v^2 + (C_3 + C_4) h + C_5 \quad (7.1)$$

$$C_1 = B \rho_i \tan^2 \phi (1 + \eta_{\mu s} \eta_{\mu c})$$

$$C_2 = C_1 \frac{\pi \rho_w \ell}{16 \rho_i}$$

$$C_3 = C \frac{\sigma_i^2}{E} B (1 + \eta_{\mu s} \eta_{\mu c})$$

$$C_4 = g(\rho_w - \rho_i) B H (\eta_{sp} + \mu \eta_{s\mu E} \frac{0.2L}{H})$$

$$C_5 = \frac{1}{4} \eta_{\mu\psi} + \eta_{\mu\theta} B \ell \rho_w g (\frac{1}{3} \ell \sin \psi + H_B W)$$

$$\eta_{sp} = \frac{\bar{S}}{H}$$

$$\eta_{s\mu E} = \frac{A_{WLF} \sin \beta}{0.2LB}$$

$$\eta_{\mu s} = \frac{1}{(\sin \phi \cos \psi)}$$

$$\eta_{\mu c} = \frac{\mu}{1 - \mu \sin \phi / \cos \psi}$$

$$\eta_{\mu\psi} = \frac{\sin \phi \cos \psi + \mu \cos^2 \phi}{\cos \psi \cos \phi - \mu \sin \phi \cos \phi}$$

$$\eta_{\mu\theta} = \sin \psi \sin \alpha + \mu \cos \alpha$$

7.2 Velocity

The ice and ship parameters are used to determine the velocity at which the ship may proceed in continuous ice. Solving Equation 7.2 for velocity, v , will give the speed in continuous ice. $R(h, v)$ is the ice resistance for continuous ice, and $T(v)$ is the thrust equation (Equation 7.3) given by Johansson [51].

$$R(h, v) - T(v) = 0 \quad (7.2)$$

$$T(v) = T_o - \frac{T_o v}{3v_o} - \frac{2T_o v^2}{3v_o^2} \quad (7.3)$$

If, when solving for v , the roots of the equation are negative or imaginary, continuous passage through the ice is not possible. In the physical sense, the thrust

available from the propellers is not enough to overcome the ice resistance and the ship will be unable to continue.

7.3 Implementation and Results

Routes were generated for two vessels, the Canadian icebreaker "Louis S. St. Laurent" and the icebreaking bulk-carrier "M.V. Arctic". The same three sets of starting and ending points from Chapter 6 are defined. Given ship parameters and ice information, the mean speed of advance across the distance represented by each pixel in the image was calculated. From the velocity and the distance, the time to travel across the pixel is found. Note that the distance through a pixel is either 12.5 meters [11] or $12.5\sqrt{2}$ meters for the diagonal.

7.3.1 Ice Parameters

The C-band image 3.2 is classified into three ice types: lead ice, first-year ice, and multi-year ice. The classification was done simply by thresholding the intensity values into three regions and using a 3×3 median filter to clean up the noisy areas. Figure 7.1 is the segmented image with white corresponding to multi-year ice, grey to first-year ice, and black to lead ice.

Table 7.1 lists the average thickness values assigned to each ice type according to data collected by Bercha [15].

The values for the ice parameters used in the calculation of ice resistance are listed in Table 7.2.

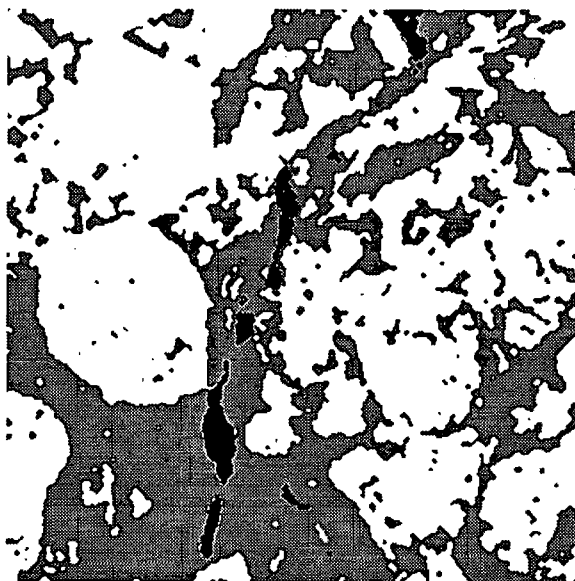


Figure 7.1: Segmentation of image chh125 into 3 ice types.

Table 7.1: Ice Thickness

Ice Type	Thickness [m]
Lead	0.2
First-year	1.8
Multi-year	2.2

7.3.2 Ship Parameters

The ship parameters for two ships, the M.V. Arctic and the Louis S. St. Laurent were compiled by Gill *et al.* [52] and are listed in Table 7.3.

7.3.3 The Routes

The travel times of the M.V. Arctic and the Louis S. St. Laurent were minimized. The same three sets of end-points from Section 6.1.2 were used. Figures 7.2, 7.3,

Table 7.2: Ice Data

Parameter	Value
σ_f	1 MPa (Gill)
E	500 MPa (Gill)
μ	0.2 (Gill)
C	5.8 (Gill)
ρ_i	900.0 kg/m^3
ρ_w	1000.0 kg/m^3

and 7.4 are the paths generated for the M.V. Arctic.

The first two paths are similar to the optimal paths generated in Chapter 6. The third path cuts through multi-year ice in order to minimize the distance. The paths consist of a number of long, straight line segments that turn abruptly. This is a result of the classified image where a pixel is classified into one of three ice thicknesses. The path continues in straight line until it hits thicker ice.

The paths for the Louis S. St. Laurent are very similar to those of the M.V. Arctic. The first path is illustrated in Figure 7.5.

Three measures of the path are listed in Table 7.4. The total distance measures the length of the path in meters, the average ice thickness gives an idea about how thick the ice was along the route, and the total transit time measures the time needed by the particular vessel to traverse the path.

7.3.4 Conclusions

From the information in Table 7.4, two conclusions are possible. First, the L.S.S. Laurent prefers to go through thicker ice in order to minimize distance. This is seen

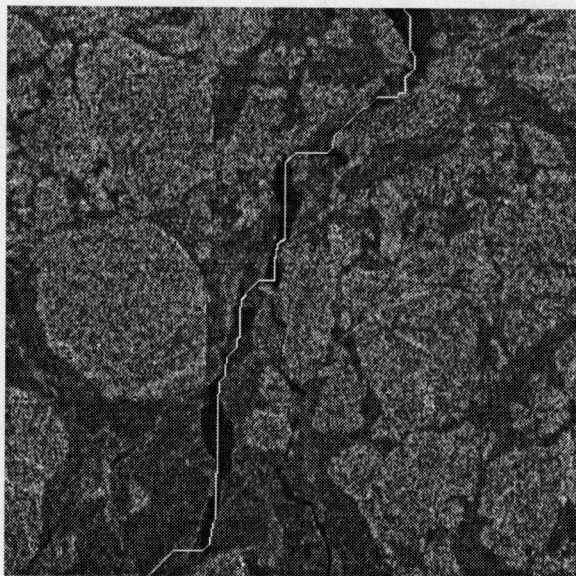


Figure 7.2: Path 1 using the transit time, M.V. Arctic.

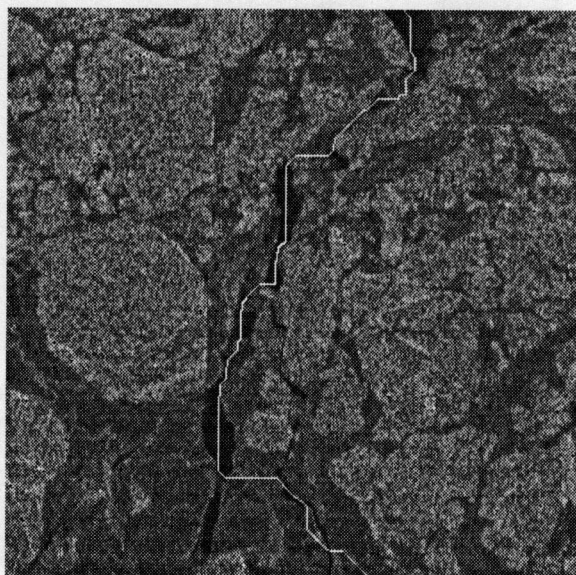


Figure 7.3: Path 2 using the transit time, M.V. Arctic.

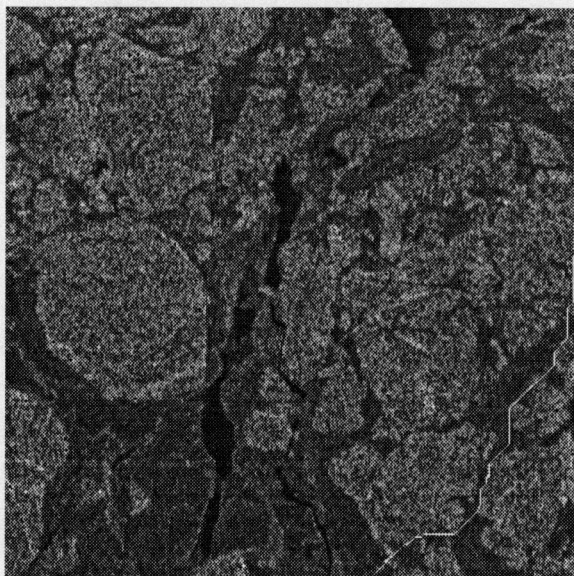


Figure 7.4: Path 3 using the transit time, M.V. Arctic.

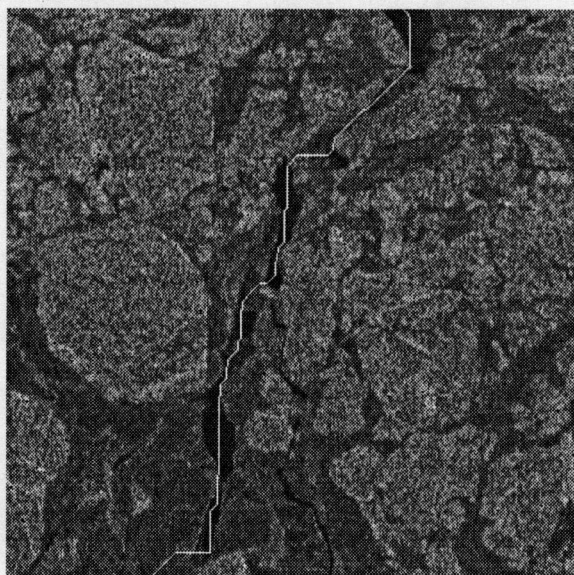


Figure 7.5: Path 1 using the transit time, L.S.S. Laurent.

Table 7.3: Ship Parameters

Parameter	M.V. Arctic	Louis S. St. Laurent
B	22.9 m	24.4 m
H	10.9 m	9.5 m
H_{BW}	0.2 m	0.2 m
L	196.7 m	111.7 m
\bar{S}	7.65 m	6.18 m
α	33°	35°
β	46°	42°
ϕ	30°	30°
ψ	53°	46°
A_{WLF}	393.9 m^2	200 m^2
T_o	$160 \times 10^3 \text{ kg}$	$230 \times 10^3 \text{ kg}$
v_o	7.72 m/s	6.69 m/s

in the results of the first two paths. Second, the results of Route 3 show that the L.S.S. Laurent is capable of proceeding with greater speed than the M.V. Arctic through non-lead ice.

7.4 Future Work

This chapter has provided a good starting point for continued effort in automatic ship routing. However, the calculation of transit time described above is approximate and includes a number of studied assumptions. The following improvements are suggested to increase the accuracy of the transit time calculation and thus improve the quality of the suggested route.

Table 7.4: Results

		Total Distance	Average Ice Thickness	Total Transit Time
M.V.	Route 1	6601m	0.87m	1497s
Arctic	2	7106m	0.97m	1719s
	3	4776m	1.87m	1817s
L.S.S.	Route1	6321m	0.89m	1221s
Laurent	2	6843m	1.03m	1232s
	3	4776m	1.87m	1817s

The accuracy of the transit time estimate is highly dependent on the quality of the data. There is a need for detailed sea ice thickness information for the planning of transportation routes. In the dynamic Beaufort Sea, sea ice is continually distorted by environmental factors such as wind and waves. Thus, the variability of the ice thickness within each ice type is not adequately represented by one average ice thickness value.

Many attempts have been made at estimating the ice thickness using imaging sensors including radar. However, due to the ambiguous correlation between ice thickness and surface characteristics, unsatisfactory results are obtained [53]. A practical tool for measuring sea ice thickness is the airborne electromagnetic induction sensor [53]. Another ice thickness measurement technique uses upward-looking sonar from submarines [54].

Ridging information is very important in planning ship routes. First-year ridges are composed of piles of loose blocks of ice. In multi-year ice, ablation has caused the ridges to become highly consolidated. Multi-year ice ridges present such a serious obstacle to ships that multi-year ice is avoided when possible. Thus, ice

data should also include the presence and thickness of ridged ice.

For the average thicknesses given in the previous examples, the thrusts of both vessels were sufficient to overcome the ice resistance. If the ship is not powerful enough to overcome the ice resistance such as when very thick ice or a ridge is encountered, the ship may resort to ramming. Ramming is a common occurrence and should be included in the determination of transit time. A number of researchers have investigated the forces present at the bow of an icebreaker during ramming [52, 55]. The ship's horizontal advance per ram, x , can be calculated using Equation 7.4 given by Gill *et al.* [52].

$$\left(\frac{1}{2}\sigma_c \tan \alpha \tan \beta\right) hx^2 - Tx - 1.2 \frac{\Delta V_r^2}{2g} + \frac{1}{2} \left(\frac{1}{\rho_w A_{WLF}} + \frac{q^2}{\Delta GM_L} \right) \left((K\sigma_f h^2)^2 \left(1 + \frac{\mu \cos \alpha}{\sin \alpha \cos \beta}\right) + 2 \frac{K\sigma_f h^2}{\cos \beta} \right) \mu T = 0 \quad (7.4)$$

σ_c is the ice compressive strength [MPa], Δ is the ship's displacement [tonnes], v_r is the ship's forward velocity during ramming [m/s], GM_L is the longitudinal metacentric height [m], q is the distance from the point of contact between the ice at the bow and the center of flotation [m], and K is a constant that varies between 0.54 and 0.67 depending on the ship[56].

Knowing the distance gained per ram, the number of rams to cross the difficult ice section can be calculated, and subsequently the time delay due to ramming can be estimated. Another ridge penetration model is given by Abdelnour *et al.* [57] where the ridges are transitted continuously with no ramming.

If the assumption of a continuous ice field is not valid, such as in an ice floe field, the ice resistance will be significantly different. In a continuous ice field, the vessel

moves forward by breaking through the ice, while in ice floe fields, the ice is pushed aside by the vessel. A number of equations have been formulated to describe the resistance in a floe field [50, 52, 58, 59].

Transit time is not the only measure of a ship's performance through a suggested route. Another measure is fuel consumption, a major factor in the cost of a marine operation. The presence of ice adds resistance which in turn leads to a higher fuel consumption rate. In addition, the presence of ice will potentially increase the voyage duration, and thus more fuel is consumed. If fuel consumption is the primary concern, the cost function should be based on the amount of fuel consumed, not travel time.

Finally, the suggested routes must be tested for safety. For instance, in a highly dynamic region, a path running through a narrow opening between two multi-year ice floes would present a large risk to ships. There is also the possibility that a section of ice has been misclassified. A path going through multi-year ice that has been misclassified poses a dangerous hazard to ship safety.

Table 7.5: Notation

Variable	Definition	Units
B	Ship beam	m
C	Coefficient dependent on type of ice failure	unitless
E	Strain modulus	MPa
g	Gravity constant	m/s
h	Ice thickness	m
H	Ship draft	m
H_{BW}	Height of bow wave	m
L	Ship Length	m
ℓ	Length of beam or width of broken cusp	m
\bar{S}	Average depth of submersion of ice	m
α	Half angle of entrance of a water line	$^\circ$
β	Angle b/w section and vertical plane	$^\circ$
ϕ	Angle b/w stem and horizontal plane	$^\circ$
ψ	Angle b/w horizontal and section perp to waterline	$^\circ$
η_{sp}	Submersion ratio = \bar{S}/H	unitless
$\eta_{s\mu E}$	Friction form coefficient = $\frac{A_{WLF} \sin \beta}{0.2LB}$	unitless
A_{WLF}	Area of water plane of entrance	m^2
$\eta_{\mu s}$	Friction form coefficient = $\frac{1}{(\sin \phi \cos \psi)}$	unitless
$\eta_{\mu c}$	Friction form coefficient = $\frac{\mu}{1 - \mu \sin \phi / \cos \psi}$	unitless
$\eta_{\mu \psi}$	Friction form coefficient = $\frac{\sin \phi \cos \psi + \mu \cos^2 \phi}{\cos \psi \cos \phi - \mu \sin \phi \cos \phi}$	unitless
$\eta_{\mu \theta}$	Friction form coefficient = $\sin \psi \sin \alpha + \mu \cos \alpha$	unitless
μ	Coefficient of friction	unitless
ρ_i	Density of ice	kg/m^3
ρ_w	Density of water	kg/m^3
σ_f	Ice flexural strength	MPa
T	Thrust	kg^3
T_o	Bollard pull	kg^3
v_o	Open water speed	m/s

Chapter 8

Summary

This report has presented a framework for developing a computer-assisted route selection system for navigation in arctic regions. The framework consists of three components: a feature extractor, a cost function, and a minimization algorithm. The feature extractor converts a synthetic aperture radar image into easily identifiable ice-types. The cost function assigns a penalty to the different ice-types which reflects the difficulty of passage. The minimization algorithm selects the route that results in the minimum total cost.

It was necessary to combine information from several research fields to successfully meet the objectives of this report. Following are the research areas that largely contributed to the solution of the problem of finding minimum-cost paths through remotely-sensed images of sea-ice.

- (i) sea ice mechanics,
- (ii) microwave remote sensing,
- (iii) operations research,
- (iv) pattern recognition, and

(v) ship-ice interaction models.

The objectives of this report were clearly met. Good routes were generated using only synthetic aperture radar images of sea-ice as input. The routes generated using the tonal feature were particularly good.

Areas for future work are easily identified. First, better features are desirable. A good feature makes the assignment of proper costs almost trivial. A good feature is characterized by a histogram where there is very little overlap between the different ice types.

Second, it is desirable to predict fuel consumption, transit time and safety factors of a proposed route. This information is reflected in the cost function used to assign costs to the pixels in the image. While this report explored the transit time through continuous ice, it would be beneficial to extend the analysis to include other ice types, as well as safety and fuel consumption factors.

Appendix A

Description of Some Sea Ice Features

A.1 First-Order Tonal Features

The following measures from Pratt [30] describe the shape of a first-order probability distribution of intensities, $P(b)$. The probability is usually estimated from the histogram.

Mean

$$\bar{b} = \sum_{b=0}^{L-1} bP(b) \quad (\text{A.1})$$

Variance

$$\sigma_b^2 = \sum_{b=0}^{L-1} (b - \bar{b})^2 P(b) \quad (\text{A.2})$$

Skewness

$$b_s = \frac{1}{\sigma_b^3} \sum_{b=0}^{L-1} (b - \bar{b})^3 P(b) \quad (\text{A.3})$$

Kurtosis

$$b_K = \frac{1}{\sigma_b^4} \sum_{b=0}^{L-1} (b - \bar{b})^4 P(b) - 3 \quad (\text{A.4})$$

Energy

$$b_N = \sum_{b=0}^{L-1} (P(b))^2 \quad (\text{A.5})$$

Entropy

$$b_E = - \sum_{b=0}^{L-1} P(b) \log_2(P(b)) \quad (\text{A.6})$$

A.2 First-Order Texture Features

Weskza et al. [35] suggest four first-order texture statistics that are computed at every pixel in the image. They are called “grey level difference statistics” and are described in Chapter 4. $P(\delta_i)$ is the probability that a difference of intensity, δ_i occurs within the neighbourhood of a pixel. L is the number of δ_i ’s which is exactly the number of grey levels in the image.

Contrast

$$CON = \sum_{\delta_i=0}^{L-1} \delta_i^2 P(\delta_i) \quad (\text{A.7})$$

The contrast is the moment of inertia about the origin. The contrast is often called Inertia.

Angular Second Moment

$$ASM = \sum_{\delta_i=0}^{L-1} P(\delta_i)^2 \quad (\text{A.8})$$

Angular second moment is at its minimum value when the probability values for each δ_i are equal. When the probability values are unequal, the ASM is larger. For instance, when the probability values are concentrated near the origin, the ASM is large. ASM is often called Energy.

Entropy

$$ENT = - \sum_{\delta_i=0}^{L-1} P(\delta_i) \log_2 P(\delta_i) \quad (A.9)$$

The entropy is at its maximum when the probability values are equal and small when they are unequal.

Mean

$$MEAN = \frac{1}{L} \sum_{\delta_i=0}^{L-1} \delta_i P(\delta_i) \quad (A.10)$$

The mean is small when the probability values are concentrated near the origin and large when the probability values are far from the origin.

A.3 Second-Order Texture Features

Haralick *et al.* [39] proposes a variety of measures that can extract useful textural information from grey level co-occurrence matrices. Three common measures are defined below.

Contrast

$$CON = \sum_{i=0}^{L-1} \sum_{j=0}^{L-1} (i-j)^2 P(i,j) \quad (A.11)$$

The contrast measures the degree of spread of the GLCM values. The greater the difference between the neighbouring grey levels, the larger the contrast value. The contrast is sensitive to both the tone and the amount of local variation in the image. Contrast is often called Inertia.

Angular Second Moment

$$ASM = \sum_{i=0}^{L-1} \sum_{j=0}^{L-1} (P(i,j))^2 \quad (A.12)$$

The ASM has the lowest value when the $P(i, j)$ are all equal; the ASM is large when some $P(i, j)$ values are high and some are low. When the image region under the moving window has grey values that are the same, or when the same (i, j) pair occur throughout the region, then one element of the GLCM will be 1 and the rest will be 0. Thus, if the image region is homogeneous or has a uniform texture, the ASM will be maximized. The ASM is sometimes called Energy or Uniformity.

Entropy

$$ENT = - \sum_{i=0}^{L-1} \sum_{j=0}^{L-1} P(i, j) \log_2 P(i, j) \quad (A.13)$$

Entropy is a measure of disorder within the window. As the image texture approaches a random state, the entropy tends towards the maximum value. The entropy value is maximum for equal $P(i, j)$ and is smaller for unequal $P(i, j)$. ENT is largest for equal $P(i, j)$ and small when they are very unequal.

Inverse Difference Moment

$$IDM = \sum_{i=0}^{L-1} \sum_{j=0}^{L-1} \frac{P(i, j)}{1 + (i - j)^2} \quad (A.14)$$

IDM assumes a larger value when the (i, j) pairs have similar grey values. A GLCM that has large near-diagonal elements will give a large IDM value. IDM is strongly but inversely related to Contrast. IDM is also known as Homogeneity.

Appendix B

Glossary of Terms

This glossary of terms has been adapted from the World Meteorological Organization Definitions of Sea Ice terms [60].

Sea ice Any form of ice found at sea which has originated from the freezing of sea water.

Ice field Area of pack ice greater than 10 km across consisting of any size of floes.

Floe Any relatively flat piece of sea ice 20 m or more across.

Fast ice Sea ice which forms and remains fast along the coast, where it is attached to the shore.

Level ice Sea ice which is unaffected by deformation.

Deformed ice A general term for ice which has been squeezed together and in places forced upwards and downwards. Subdivisions are rafted ice, ridged ice and hummocked ice.

Ice pressure Caused by compaction of ice floes under the influence of wind or water currents, forming ice deformation of several forms (fractures, hummocks, ridges, rafting).

Ice concentrations A ratio expressed in tenths describing the amount of the water surface covered by ice as a fraction of the whole area.

Open water A large area of freely navigable water in which ice is present in concentrations less than 1/10. No ice of land origin is present.

Pack ice Floating ice in which the concentration is 7/10 to 10/10. The concentration ranges from floes mostly in contact with one another to floes which are frozen together.

Consolidated ice Floating ice in which the concentration is 10/10 and the floes are frozen together.

Crack Any fracture of fast ice, consolidated ice, or a single floe which may have been followed by separation ranging from a few centimeters to 1 m.

Ice edge The demarcation at any given time between the open water and sea, lake or river ice whether fast or drifting. May be termed compacted or diffuse.

Young ice A general term for recently formed ice, 0-30 cm thick, which includes new ice, grey ice, and grey-white ice.

New ice This type of ice is composed of ice crystals which are only weakly frozen together.

Grey ice Young ice 10-15 cm thick. Less elastic than new ice and breaks on swell. Usually rafts under pressure.

Grey-white ice Young ice 15-30 cm thick. Under pressure it is more likely to ridge than to raft.

First-year ice Ice of not more than one winter's growth, 30-200 cm thick.

Multi-year ice Sea ice which has survived at least one summer's melt. Topographic features generally are smoother than first-year ice.

Hummock A hillock of broken ice which has been forced upwards by pressure. May be fresh or weathered.

Lead Any fracture or passage-way through sea ice which is navigable by surface vessels.

Rafted ice Type of deformed ice formed by one piece of ice overriding another.

Ridge A line or wall of broken ice forced up by pressure. May be fresh or weathered.

Shearing An area of pack ice is subject to shear when the ice motion varies significantly in the direction normal to the motion, subjecting the ice to rotational forces.

Diverging Ice fields or floes in an area are subjected to diverging or dispersive motion, thus reducing concentration and/or relieving stresses in the ice.

Compacting Pieces of floating ice are said to be compacting when they are subjected to a converging motion which increases ice concentration and/or produces stresses which may result in ice deformation.

Fracture Any break or rupture through pack ice or a single floe resulting from deformation processes.

Weathering Processes of ablation and accumulation which gradually eliminate irregularities in an ice surface.

Beset Situation of a vessel surrounded by ice and unable to move.

Ice under pressure Ice in which deformation processes are actively occurring and hence a potential impediment or danger to shipping.

Bibliography

- [1] C. Gautier. Functional specifications for second-generation ice navigation system. Technical report, Canarctic Shipping Company Ltd., 1990.
- [2] R. Onstott. Active microwave classification of sea ice. *Proceedings of IGARSS '89 Symposium*, pages 369–371, 1989.
- [3] E. O. Lewis, B. W. Currie, and S. Haykin. *Detection and Classification of Ice*. Research Studies Press Ltd, Letchworth, first edition, 1987.
- [4] E. Williams, C. Swithinbank, and G. de Q. Robin. A submarine study of arctic pack ice. *Journal of Glaciology*, 15(1):349–362, 1975.
- [5] G. Maykut. The ice environment. In R. Horner, editor, *Sea Ice Biota*, pages 21–82. CRC Press, 1985.
- [6] W. Tucker, D. Perovich, A. Gow, W. Weeks, and M. Drinkwater. Physical properties of sea ice relevant to remote sensing. In F. Carsey, editor, *Microwave Remote Sensing of Sea Ice*, pages 9–28. American Geophysical Union, 1992.
- [7] R. G. Onstott. SAR and scatterometer signatures of sea ice. In F. Carsey, editor, *Microwave Remote Sensing of Sea Ice*, pages 73–103. American Geophysical Union, 1992.

- [8] B. W. Currie, T. O. Greenlay, and S. Haykin. *Evaluation of radar techniques as they apply to the detection and clasification of sea ice*. Communications Research Laboratory, McMaster University, Hamilton, first edition, 1981.
- [9] D. Held, W. Brown, A. Freeman, J. Klein, H. Zebker, T. Sato, T. Miller, Q. Nguyen, and Y. Lou. The NASA/JPL multifrequency, multipolarisation airborne SAR system. *Proceedings of IGARSS '88 Symposium*, pages 345-349, 1988.
- [10] M. Drinkwater and J. Crawford. Multi-frequency, multi-polarization SAR and radiometer sea ice classification. *Proceedings of IGARSS '91 Symposium*, pages 107-111, 1991.
- [11] T. Falco, F. Francis, S. Lovejoy, D. Schertzer, B. Kerman, and M. Drinkwater. Universal multifractal scaling of synthetic aperture radar images of sea-ice. *IEEE Transactions on Geoscience and Remote Sensing*, pages 906-909, 1996.
- [12] J. Marko. Satellite observations of the Beaufort sea ice cover. Technical Report 34, Institute of Ocean Science, Victoria, B.C., 1975.
- [13] T.J.O. Sanderson. *Ice Mechanics: Risks to Offshore Structures*. Graham and Trotman, London, first edition, 1988.
- [14] E. Rignot and R. Kwok. Characterization of spatial statistics of distributed targets in SAR data. *International Journal of Remote Sensing*, 14(2):345-363, 1993.
- [15] F. Bercha. Ice-structure interaction: Engineering design and construction criteria. Technical report, Public Works Canada, Ottawa, 1985.

- [16] M. Drinkwater, R. Kwok, E. Rignot, H. Israelsson, R. Onstott, and D. Winebrenner. Potential applications of polarimetry to the classification of sea ice. In F. Carsey, editor, *Microwave Remote Sensing of Sea Ice*, pages 419–429. American Geophysical Union, 1992.
- [17] B. Kerman. Information states in sea ice imagery. To be published, 1996.
- [18] B. Ramsay, T. Hirose, M. Manore, J. Falkingham, R. Gale, D. Barber, M. Shokr, B. Danielowicz, B. Gorman, and C. Livingstone. Potential of RADARSAT for sea ice applications. *Canadian Journal of Remote Sensing*, 19(4):352–360, 1993.
- [19] C. Wackerman and C. Jentz. Sea ice classification of SAR imagery. *Proceedings of IGARSS '88 Symposium*, pages 425–427, 1988.
- [20] D. Haverkamp, L. Soh, and C. Tsatsoulis. A comprehensive, automated approach to determining sea ice thickness from sar data. *IEEE Transactions on Geoscience and Remote Sensing*, 33(1):46–57, 1995.
- [21] D.G. Barber. Texture measures for SAR sea ice discrimination. Technical report, Institute for Space and Terrestrial Science, University of Waterloo, 1989.
- [22] D.G. Barber and E.F. LeDrew. SAR sea ice discrimination: A multivariate approach. *Photogrammetric Engineering Remote Sensing*, 57(4):385–395, 1991.
- [23] D.G. Barber, M.E. Shokr, R.A. Fernandes, E.D. Soulis, D.G. Flett, and E.F. LeDrew. A comparison of second-order classifiers for SAR sea ice discrimination. *Photogrammetric Engineering Remote Sensing*, 59(9):1397–1408, 1993.

- [24] J. Nystuen and F. Garcia. Sea ice classification using SAR backscatter statistics. *IEEE Transactions on Geoscience and Remote Sensing*, 30:503–509, 1992.
- [25] R. Shuchman, C. Wackerman, A. Maffett, R. Onstott, and L. Sutherland. The discrimination of sea ice types using SAR backscatter statistics. *Proceedings of IGARSS '89 Symposium*, pages 381–385, 1989.
- [26] Q. Holmes, D. Nuesch, and R. Shuchman. Textural analysis and real-time classification of sea ice types using digital SAR data. *IEEE Transactions on Geoscience and Remote Sensing*, 22(2):113–120, 1984.
- [27] M.E. Shokr. Texture measures for sea-ice classification from radar images. *Proceedings of IGARSS '89 Symposium*, pages 763–768, 1989.
- [28] B. Guindon, R. Hawkins, and D. Goodenough. Spectral-spatial analysis of microwave sea ice data. *Proceedings of the International Geoscience and Remote Sensing Symposium*, page ., 1982.
- [29] J. Lyden, B. Burns, and A. Maffett. Characterization of sea ice types using synthetic aperture radar. *IEEE Transactions on Geoscience and Remote Sensing*, 22(5):431–439, 1984.
- [30] W. K. Pratt. *Digital Image Processing*. John Wiley and Sons, New York, first edition, 1978.
- [31] J.K. Hawkins. *Textural Properties for Pattern Recognition*. B. Lipkin and A. Rosenfeld (editors), Academic Press, New York, first edition, 1969.
- [32] H. Tamura, S. Mori, and Y. Yamawaki. Textural features corresponding to visual perception. *IEEE Transactions on Systems, Man, and Cybernetics*, SMC-8(6):460–473, 1978.

- [33] L. Van Gool, P. Dewaele, and A. Oosterlinck. Texture analysis anno 1983. *Computer Vision*, 29(6):336–357, 1985.
- [34] R.M. Haralick. Statistical and structural approaches to texture. *Proceedings of the IEEE*, 67(5):786–804, 1979.
- [35] J. Weszka, C. Dyer, and A. Rosenfeld. A comparative study of texture measures for terrain classification. *IEEE Transactions on Systems, Man, and Cybernetics*, SMC-6(4):269–285, 1976.
- [36] H. Wechsler. Texture analysis - A survey. *signal Processing*, 2(3):271–282, 1980.
- [37] C. Sun and W.G. Wee. Neighbouring grey level dependence matrix for texture classification. *Computer Vision, Graphics and Image Processing*, 23:341–352, 1982.
- [38] M. Amadasun and R. King. Textural features corresponding to textural properties. *IEEE Transactions on Systems, Man, and Cybernetics*, 19(5):1264–1274, 1989.
- [39] R.M. Haralick, K. Shanmugam, and I. Dinstein. Textural features for image classification. *IEEE Trans. on Systems, Man, and Cybernetics*, SMC-3(6):610–621, 1973.
- [40] M.E. Shokr. Evaluation of second-order texture parameters for sea ice classification from radar images. *Journal of Geophysical Research*, 96(6):10625–10640, 1991.
- [41] B. Kerman. An informational energetics formulation of damage in sea ice imagery. Accepted for publication in *Nonlinear Processes Geophysics*, 1996.

- [42] B. Kerman and K. Johnson. Experimental evaluation of a markov-gibbs model for sea ice imagery. Submitted to *Nonlinear Processes Geophysics*, 1996.
- [43] J. Eklundh. On the use of Fourier phase features for texture discrimination. *Computer Graphics and Image Processing*, 9(2):199–201, 1979.
- [44] R.W. Connors and C.A. Harlow. A theoretical comparison of four texture algorithms. Technical report, The College of Engineering, University of Missouri-Columbia, 1976.
- [45] M. Galloway. Texture analysis using grey level run lengths. *Computer Graphics and Image Processing*, 4:172–199, 1975.
- [46] E.W. Dijkstra. A note on two problems in connection with graphs. *Numerische Mathematik*, 1(1):269–271, 1959.
- [47] F. Chu. Ship resistance in homogeneous ice fields. Technical report, Helsinki University of Technology, 1976.
- [48] G. Lindqvist. A straightforward method for calculation of ice resistance of ships. In *International Conference on Port and Ocean Engineering under Arctic Conditions*, volume 2, pages 722–735, 1989.
- [49] E. Enkvist. On the ice resistance encountered by ships operating in continuous mode of ice breaking. Technical Report 24, The Swedish Academy of Engineering Sciences in Finland, Helsinki, 1972.
- [50] V.I. Kashteljan, I.I. Poznyak, and A.Y. Ryvlin. Ice resistance to motion of a ship (translation). *Sudstroenic*, 1(1), 1968.

- [51] B.M. Johansson. Economics of winter navigation in the northern part of gulf of bothnia. Technical Report 20, Finnish-Swedish Winter Navigation Research Board, 1977.
- [52] R.J. Gill, A. Aboul-Azm, B.F. Terry, and W.E. Russell. A ship transit model for passage through ice and its application to the labrador area. In *Ship Technology and Research Symposium*, volume 6, pages 105–112, 1981.
- [53] J. Rossiter and J. Holladay. Ice-thickness measurement. In S. Haykin, E. Lewis, R. Raney, and J. Rossiter, editors, *Remote Sensing of Sea Ice and Icebergs*, pages 141–173. John Wiley and Sons, Inc., 1994.
- [54] P. Wadhams. Sea ice morphology and its measurement. In I. Dyer and C. Chrysostomidis, editors, *Arctic Technology and Policy*, pages 179–195. Hemisphere Publishing Corporation, 1984.
- [55] R.M. White. *Dynamically Developed Force at the Bow of an Icebreaker*. PhD thesis, MIT, 1965.
- [56] B. Michel. *Ice Mechanics*. Les Presses de l'Universite Laval, Quebec, 1 edition, 1978.
- [57] R. Abdelnour, G. Comfort, and T. Peirce. Single pass ridge penetration model. In *International Conference on Port and Ocean Engineering under Arctic Conditions*, volume 2, pages 600–616, 1991.
- [58] Y.N. Popov, D.V. Faddeev, D.Y. Kheisin, and A.A. Yakolev. Durability of ships designed for ice passage (translation). *Sudstroenic*, 1(1), 1968.
- [59] R.A. Major, D.M. Berenger, and C.J. Lawrie. A model to predict hull-ice impact loads in the St. Lawrence. In *Ice Tech 75*, volume 1, 1975.

- [60] Environment Canada. Manice - manual of sea ice reporting. Technical report, Atmospheric Environment Canada, 1980.